Journal of Structural Geology 32 (2010) 70–85

Contents lists available at ScienceDirect

Journal of Structural Geology

journal homepage: www.elsevier.com/locate/jsg

Middle crustal ductile deformation patterns in southern Tibet: Insights from vorticity studies in Mabja Dome

Jackie Langille[a,*], Jeffrey Lee[a], Bradley Hacker[b], Gareth Seward[b]

[a] Department of Geological Sciences, Central Washington University, Ellensburg, WA 98926, USA
[b] Department of Earth Science, University of California, Santa Barbara, CA 93106, USA

ARTICLE INFO

Article history:
Received 24 November 2008
Received in revised form
13 June 2009
Accepted 9 August 2009
Available online 14 August 2009

Keywords:
Channel-flow
Himalaya
Mabja Dome
Microstructures
Middle crust
Tibet
Vorticity

ABSTRACT

Kinematic, kinematic vorticity (W_m), and deformation-temperature analyses were performed to test the hypothesis that mid-crustal rocks exposed in Mabja Dome, southern Tibet, were penetratively deformed within a southward-flowing mid-crustal channel during the late Eocene/early Oligocene to early Miocene. Outcrop and thin-section kinematic indicators show a downward transition from mixed top-N and top-S shear in chloritoid- and garnet-zone rocks, through dominantly top-S shear in garnet- and kyanite-zone rocks, to solely top-S shear in staurolite-zone and deeper rocks. Along mineral elongation lineation-parallel transects, W_m in schists and orthogneisses decreases with structural depth from ~0.80 (~40% pure shear) to ~0.55 (~63% pure shear). Deformation temperature increases from ~450 °C in the chloritoid-zone to >700 °C in the sillimanite-zone, coincident with peak metamorphic temperatures, indicating that W_m was recorded during peak metamorphism. These mid-crustal rocks thus exhibit deformational patterns characterized by: (1) locally opposing shear sense suggesting bulk pure shear at moderate structural depths; (2) a broad top-S shear zone above the Main Central Thrust; and (3) increasing pure shear with structural depth, suggesting an increase in lithostatic load. Our results from mid-crustal rocks exposed in the core of Mabja Dome yield patterns of ductile deformation in southern Tibet that define non-ideal channel flow.

1. Introduction

The Himalayan orogen records Eocene to Holocene continental collision and convergence between the Indian and the Eurasian plates. Profound crustal shortening and thickening formed one of the most impressive orogenic belts on Earth: the Himalaya, with a length of ~2500 km and 14 peaks over 8000 m in elevation, and the Tibetan Plateau, Earth's largest plateau, which covers $>5 \times 10^6$ km^2 and has an average elevation of ~5000 m (Fielding et al., 1994).

Extensive geologic and geophysical research over the last 15–20 years has focused on characterizing: (1) the development and outward growth of the Tibetan Plateau (e.g. Grujic et al., 1996, 2002; Vannay and Grasemann, 1998; Grasemann et al., 1999; Hodges et al., 2001); (2) the development of partial melt zones interpreted to reside in the present-day middle crust of Tibet (e.g. Nelson et al., 1996); (3) the development of structures along the southern margin of the plateau, including the broadly coeval South Tibetan Detachment System (STDS) and Main Central Thrust (MCT) that bound the high-grade Greater Himalayan sequence (GHS) (Fig. 1) (e.g. Grujic et al., 1996, 2002; Vannay and Grasemann, 1998; Grasemann et al., 1999); (4) southward extrusion of the GHS (e.g. Grujic et al., 1996, 2002; Vannay and Grasemann, 1998; Grasemann et al., 1999; Beaumont et al., 2001, 2004, 2006); and (5) focused erosion along the southern margin of the plateau (e.g. Burbank et al., 1996; Beaumont et al., 2001; Hodges et al., 2001). In aggregate, the results from these studies formed the foundation of the channel-flow hypothesis (e.g. Beaumont et al., 2001; Hodges et al., 2001) (Fig. 2). For example, Grujic et al. (1996) used quartz microfabrics from Bhutan to demonstrate general non-coaxial flow of the GHS, and postulated that the GHS deformed as a wedge between the MCT and STDS; later, Grujic et al. (2002) reformulated this wedge model by postulating that the GHS deformed as a 10–15 km thick channel that extends >200 km northward beneath Tibet. Vannay and others (i.e. Vannay and Grasemann, 1998, 2001; Grasemann et al., 1999) used a combination of spatially varying kinematic vorticity numbers (defined below) and deformation temperatures, metamorphic pressure/temperature (P–T) conditions associated with inverted isograds, and mica $^{40}Ar/^{39}Ar$ cooling ages from the base of the GHS in the Sutlej Valley to reach similar conclusions.

* Corresponding author at: Department of Earth and Planetary Sciences, University of Tennessee, Knoxville, TN 37996, USA.
E-mail address: jlangill@utk.edu (J. Langille).

0191-8141/$ – see front matter © 2009 Elsevier Ltd. All rights reserved.
doi:10.1016/j.jsg.2009.08.009

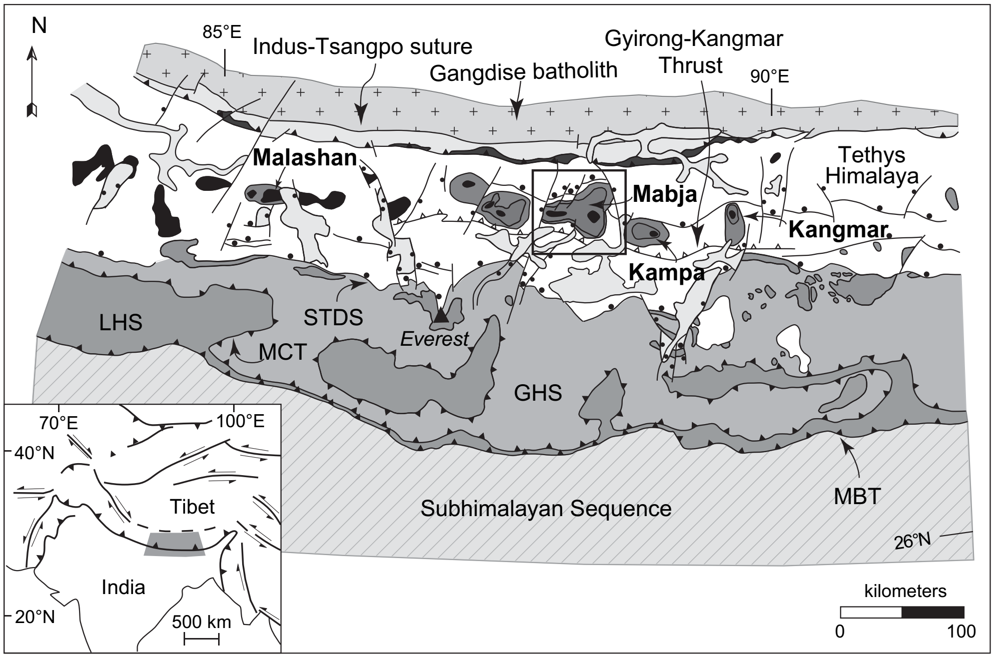

Fig. 1. Regional tectonic map of the south-central Himalayan orogen. Leucogranites (black) and high- and low-grade metamorphic rocks (dark gray) of the North Himalayan gneiss domes, including Mabja Dome, are shown with respect to major geologic features such as the Main Boundary Thrust (MBT), Main Central Thrust (MCT), Greater Himalayan Sequence (GHS), Lesser Himalayan Sequence (LHS), and South Tibetan Detachment System (STDS). Inset map shows the regional location of the detailed map; box shows location of index map in Fig. 4. Modified from Lee et al. (2004).

These data and ideas have since been incorporated into a set of transient, plane-strain, finite-element models in which the GHS represents a 15–30 km thick, hot, low-viscosity middle-crust channel that extrudes southward from beneath Tibet toward the orogenic front during north–south convergence (Fig. 2; Beaumont et al., 2001, 2004, 2006). In these models, south-directed flow begins after the crust has been tectonically thickened and the middle crust experiences a reduction in viscosity as a consequence of partial melting due to mantle heat flux and crustal radiogenic heating. Flow and extrusion of the low-viscosity tabular body of middle crust is driven by a horizontal gravitational potential-energy gradient produced by the topographic and crustal thickness differences between the Tibetan Plateau and its margins and enhanced focused erosion along the southern flank of the high Himalaya (e.g. Beaumont et al., 2001, 2004; Hodges et al., 2001). The low-viscosity channel is bounded above and below by normal-sense (STDS) and thrust-sense (MCT) shear zones, respectively, that separate the channel from higher viscosity material above and below (Beaumont et al., 2001, 2004) (Figs. 1 and 2).

Flow within a channel can range from pure Poiseuille flow (Fig. 3A) to a combination of Poiseuille and Couette flow (Fig. 3B). Poiseuille (or parabolic) flow develops between stationary rigid plates in which a horizontal gradient in lithostatic pressure and frictional resistance along the boundaries produces the greatest velocities in the center of the channel and decreasing velocities toward the top and bottom of the channel, leading to development of opposing shear sense. Poiseuille flow is characterized by a simple shear (large vorticity number (W_m)) at the top and bottom of the channel, general shear toward the center of the channel (decreasing W_m), and pure shear at the center of the channel (small W_m) (Fig. 3). Couette (or linear) flow develops between rigid plates moving relative to one another and is characterized by simple shear across the channel (e.g. White, 1974; Grujic, 2006) (Figs. 2 and 3).

Thermal–mechanical models have been derived principally from geophysical data from southern Tibet and geological data from the Himalayan front. Absent are geological data north of the Himalaya, closer to the presumed source of flowing crust. Data on the style, W_m, and spatial distribution of mid-crustal flow in southern Tibet are essential for testing the proposed link between mid-crustal channel-flow and denudation-driven extrusion. Mabja Dome, southern Tibet, one of the North Himalayan gneiss domes (Fig. 1), is an ideal location for such investigations. This dome, ~100 km north of the high Himalaya, provides excellent exposure of an originally ~35-km thick sequence of middle crustal rocks that preserve mid-crustal deformational fabrics that predate doming and for which pressure/temperature/time data are well known (Lee et al., 2004, 2006; Zhang et al., 2004; Lee and Whitehouse, 2007). To document patterns of channel flow, we completed detailed kinematic, microstructural, and vorticity investigations on metamorphic mid-crustal rocks exposed in the core of Mabja Dome. Our

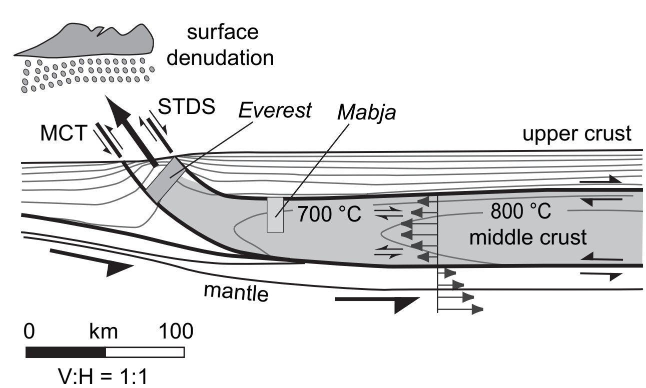

Fig. 2. Schematic diagram of a southward-flowing low-viscosity middle crustal channel (gray) bounded by the STDS and the MCT. Poiseuille flow dominates within the channel and Couette flow beneath the channel (see Fig. 3). Predicted locations of middle crustal rocks exposed in Mabja Dome and of the Greater Himalayan sequence in the Everest region prior to exhumation are shown. Double-barbed arrows indicate velocity vectors; single-barbed arrows indicate relative sense of displacement; rain drops indicate erosion. Modified from Beaumont et al. (2004) and Godin et al. (2006).

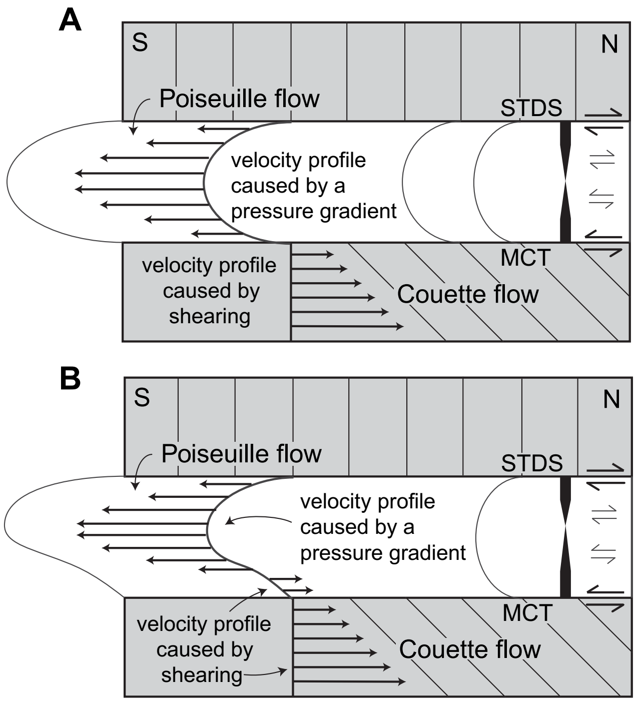

Fig. 3. (A) Velocity profile of idealized channel flow in the middle crust of southern Tibet. Poiseuille flow, driven by a horizontal lithostatic pressure gradient, and Couette flow, driven by shearing, are shown by arrows depicting velocity vectors. (B) Velocity profile of hybrid channel flow in the middle crust of southern Tibet driven by a combination of Poiseuille and Couette flow within the channel. Double-barbed arrows indicate velocity vectors; single-barbed arrow pairs indicate shear sense; vorticity (W_m, black column) decreases from 1.0 (simple shear; wide part of the column) at the edges of the channel to 0 (pure shear; narrow part of the column) toward the center of the channel; dark gray bounding plates are rigid. Modified from Ramsay and Huber (1987) and Grujic et al. (2002).

results show that the patterns of ductile deformation in the middle crust of southern Tibet define non-ideal channel flow compared to the patterns of ductile deformation predicted by the channel-flow models.

2. Geologic setting

2.1. Regional geology

The North Himalayan gneiss domes are exposed approximately halfway between the Indus–Tsangpo suture to the north and the STDS to the south within the Tethys Himalaya, an unmetamorphosed to weakly metamorphosed sedimentary series (Fig. 1). The Tethys Himalaya is underlain by Proterozoic to Jurassic pre-, syn-, and post-rift sedimentary rocks, a Jurassic to Cretaceous passive continental margin sedimentary sequence, and an upper Cretaceous to Eocene syn-collisional sedimentary sequence deposited on the northern margin of the Indian continent (Gansser, 1964; Le Fort, 1975; Gaetani and Garzanti, 1991; Brookfiel, 1993; Liu and Einsele, 1994; Garzanti, 1999). The Tethys Himalaya is structurally complex, exhibiting Cretaceous to Holocene contractional and extensional structures in a variety of orientations. The first major north–south contractional event is Paleocene to early Eocene in age (Burg et al., 1984; Burg and Chen, 1984). A second, younger post-collisional contractional deformational event in the northern portion of the Tethys Himalaya is characterized by east–west-striking thrust faults and folds and an increase in strain toward the south-directed Gyirong–Kangmar thrust fault (GKT) (Fig. 1) (Burg and Chen, 1984; Ratschbacher et al., 1994). Based on mica $^{40}Ar/^{39}Ar$ cooling ages in the core of the Kangmar Dome, Burg and Chen (1984), Burg et al. (1987), and Lee et al. (2000) inferred middle Miocene slip along the GKT. These older structures are cut by middle Miocene and Pliocene to Holocene north–south-striking grabens (e.g. Armijo et al., 1986; Wu et al., 1998; Stockli et al., 2002; Dewane et al., 2006; Hager et al., 2006).

2.2. Geology of Mabja Dome

Geologic studies of North Himalayan gneiss domes have focused largely on the Kangmar, Kampa, Mabja, and Malashan domes (Fig. 1) (e.g. Burg et al., 1984; Chen et al., 1990; Lee et al., 2000, 2002, 2004, 2006; Zhang et al., 2004; Aoya et al., 2005, 2006; Quigley et al., 2006, 2008; Lee and Whitehouse, 2007). The domes generally consist of a core of orthogneisses, migmatites, leucogranites, and high-grade metasedimentary rocks overlain by progressively lower-grade to unmetamorphosed sedimentary rocks (e.g. Burg et al., 1984; Chen et al., 1990; Lee et al., 2000, 2004, 2006; Aoya et al., 2005, 2006; Quigley et al., 2006; Kawakami et al., 2007).

Mabja Dome is characterized by a core of Tertiary migmatitic orthogneiss mantled by Paleozoic orthogneiss and metasedimentary rocks that in turn are overlain by Triassic and Jurassic metasedimentary and sedimentary rocks. At the base of the section is a late Eocene/early Oligocene K-feldspar augen + biotite + plagioclase + quartz ± muscovite ± sillimanite ± garnet-bearing granitic migmatite orthogneiss (unit EOg, Fig. 4) (Lee et al., 2004; Lee and Whitehouse, 2007). The top of this basal orthogneiss is an intrusive contact into overlying metapelite. Structurally overlying EOg is a moderately well-exposed Paleozoic orthogneiss and paragneiss complex (unit Pop, Fig. 4) composed of dominantly K-feldspar granitic augen gneiss with horizons of quartz + muscovite + biotite + plagioclase ± garnet ± kyanite ± staurolite ± sillimanite schist (Lee et al., 2004). Structurally above Pop is a Paleozoic schist, marble, and quartzite sequence (units Pls, Pm, Pus, and Pq; Fig. 4). This sequence grades upward into a sequence of Triassic graphite-rich siliciclastic rocks (unit Ts, Fig. 4) (Lee et al., 2004). Metamorphic grade within the Ts unit decreases upsection from garnet-zone at the base to unmetamorphosed sandstone, siltstone, and argillite at the top. During the Miocene these rocks were intruded by amphibolite dikes, a pegmatite and aplite dike swarm, two-mica granites, and a single rhyolite porphyry dike (Figs. 4 and 5) (Lee et al., 2004, 2006; Lee and Whitehouse, 2007).

Rocks in Mabja Dome record evidence from three major deformational events: D1, characterized by north–south shortening and vertical thickening; D2, characterized by vertical thinning and north–south extension associated with moderate temperature/pressure metamorphism and intrusion of leucogranites; and a younger doming event (Lee et al., 2004). D1, the oldest deformational event, is best exposed and dominant at the highest structural levels where it is characterized by east–west-trending F1 folds that shortened bedding horizontally. Superimposed on the D1 structural fabrics is D2, a high-strain deformational event that is manifested at higher structural levels as an S2 crenulation cleavage developed at large angles to S1. Strain associated with D2 increases down structural section such that below the garnet-in isograd, bedding and the S1 foliation have been transposed parallel to a mylonitic S2 foliation. The S2 mylonitic foliation is defined by aligned micas, weakly to strongly flattened quartz grains, and mica and quartz segregations (Lee et al., 2004). Associated with the high-strain S2 foliation is a well-developed ∼north–south trending mineral elongation lineation, L2, defined by smeared biotite, ribbon quartz grains, and strain shadows on augen and porphyroblasts. The combination of a well-developed foliation and elongation lineation indicates approximately plane strain (Lee et al., 2004). Subsequent to the formation

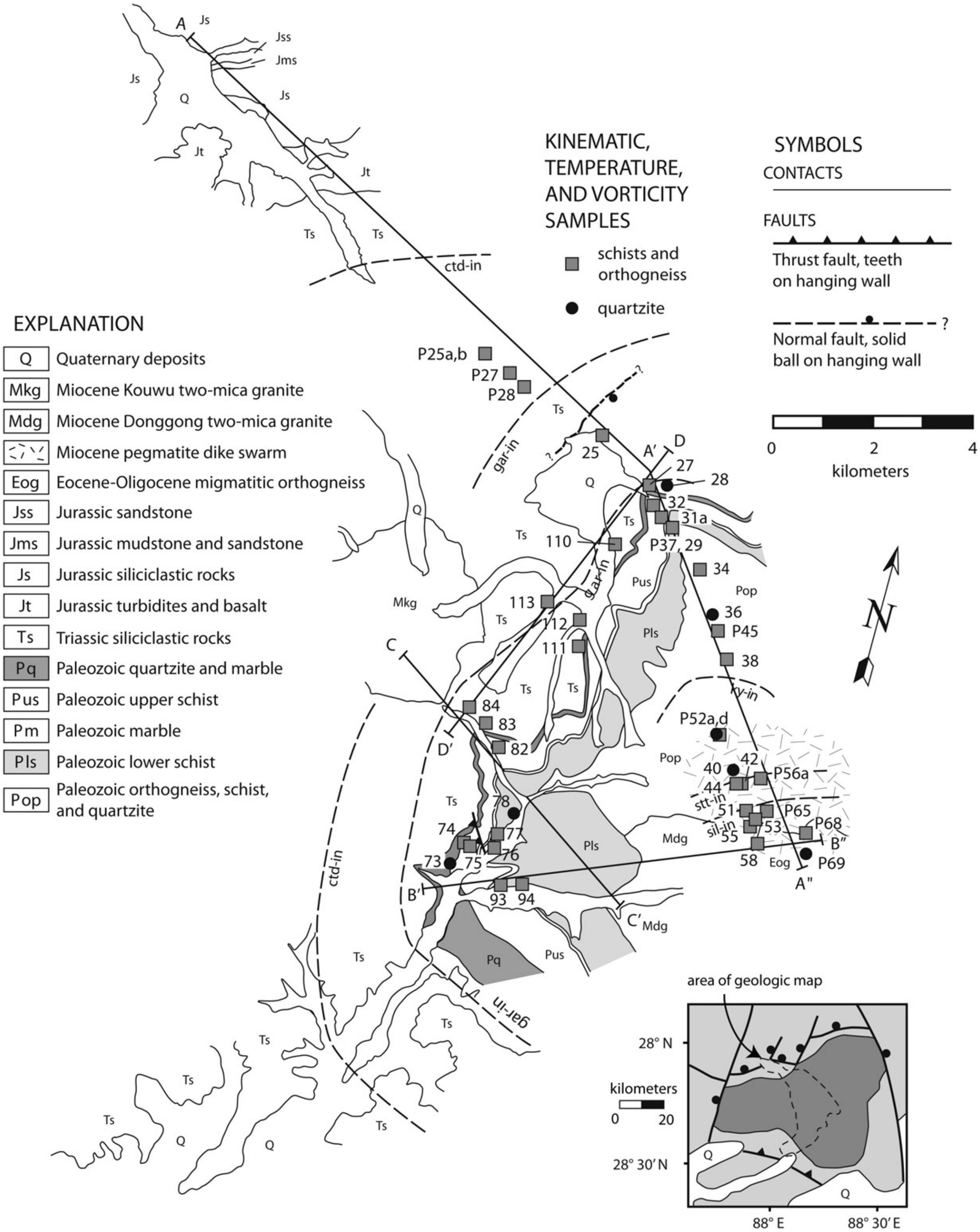

Fig. 4. Simplified geologic map (modified from Lee et al., 2004) showing kinematic, deformation temperature, and vorticity sample locations and metamorphic isograds (bold dashed lines). Ctd, chloritoid; gar, garnet; ky, kyanite; stt, staurolite; sill, sillimanite. Index map shows location of Mabja Dome geologic map (dashed line) (see Fig. 1); metamorphic core, medium gray; unmetamorphosed Tethyian sediments, light gray.

of D2 fabrics, the S2 foliation was domed into a doubly plunging, antiformal dome (Lee et al., 2004).

Microstructures indicate that peak metamorphism occurred after D1 deformation and prior to or during D2 deformation (Lee et al., 2004). Metasedimentary rocks preserve Barrovian peak metamorphism defined by mineral assemblages (chloritoid-, garnet-, kyanite-, staurolite-, and sillimanite-in isograds) that increase in grade toward the center of the dome (Figs. 4 and 5). Based on mineral assemblages and quantitative thermobarometry, Lee et al. (2004) inferred temperatures and pressures of ∼475–

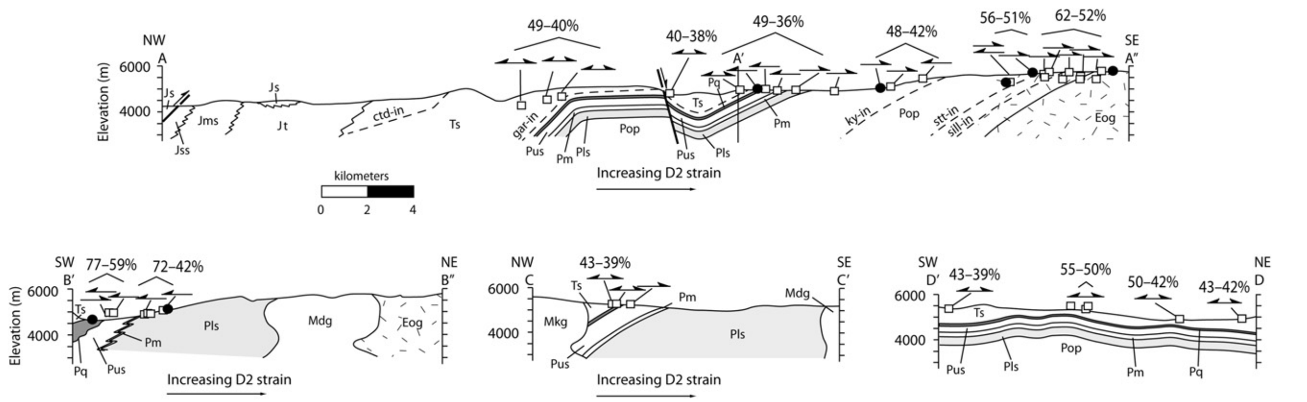

Fig. 5. Sample locations, metamorphic isograds, percent pure shear, and shear-sense arrows projected onto cross sections approximately parallel to the D2 mineral elongation lineation (A-A′-A″ and C–C′) and nearly perpendicular to the D2 mineral elongation lineation (B–B′ and D–D′). Single-barbed arrow, top relative to bottom sense of shear; double-barbed arrow, opposing top relative to bottom senses of shear. Cross section locations and explanation shown in Fig. 4. Cross sections A–A′–A″ and B′–B″ modified from Lee et al. (2004).

530 °C and ~150–450 MPa for the chloritoid-zone and calculated temperatures that increase from 575 ± 50 °C in the garnet-zone to 705 ± 65 °C in the sillimanite-zone; pressures from garnet-, staurolite-, and sillimanite-zone rocks are constant at ~800 MPa, regardless of structural depth. Lee et al. (2004) estimated that the metamorphic rocks were vertically thinned by ~50–10% based on the gradient in metamorphic pressure between the chloritoid-in isograd and garnet-zone rocks.

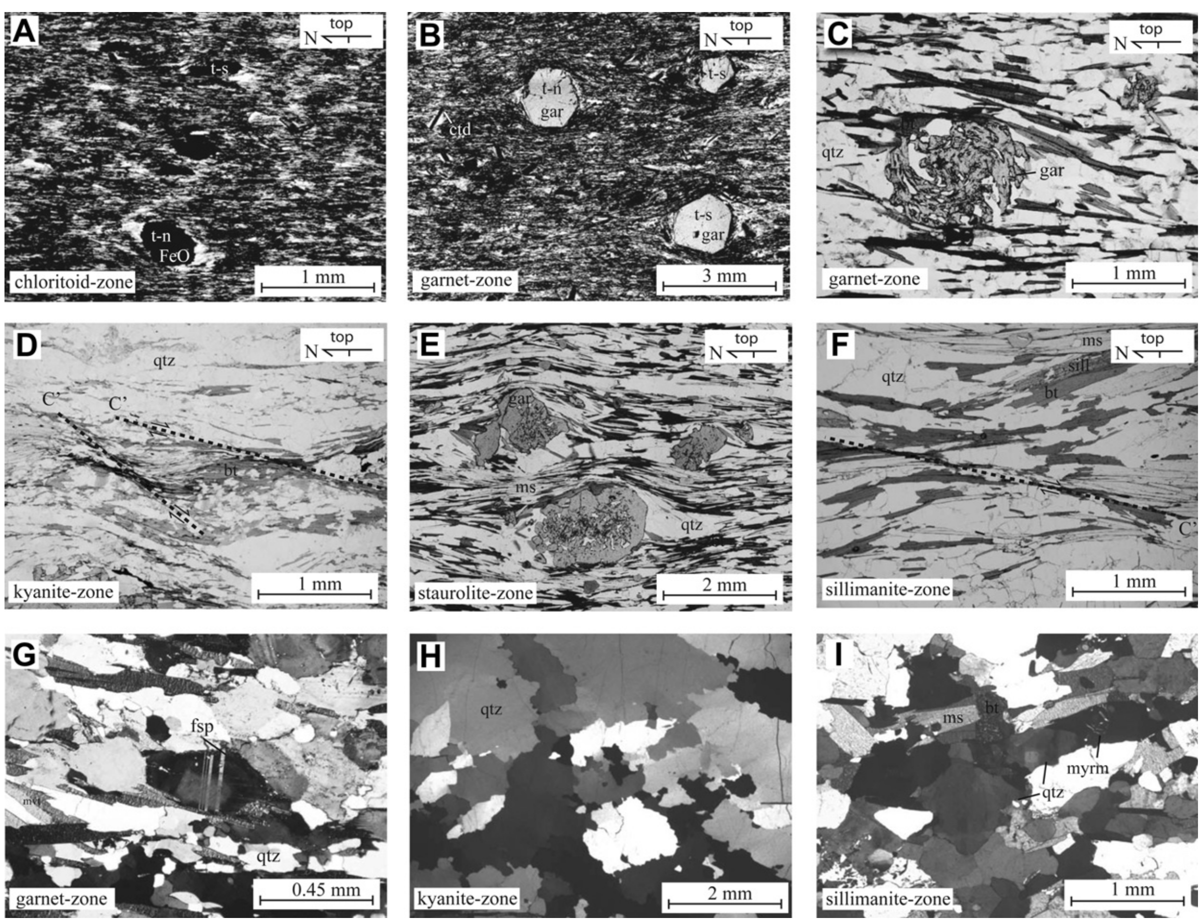

Fig. 6. Photomicrographs of microstructures, (A) through (F), and quartz and feldspar deformation textures, (G) through (I). (A) Chloritoid-zone schist containing chloritoid porphyroblasts and rotated iron-oxide (FeO) porphyroblasts which exhibit top-N (t-N) and top-S (t-S) shear; plane light. (B) Garnet-zone schist containing garnet (gar) porphyroblasts which exhibit top-N and top-S shear; ctd, chloritoid; plane light. (C) Garnet-zone schist containing a garnet porphyroclast exhibiting rotated inclusion patterns indicating top-N shear; plane light. (D) Kyanite-zone schist exhibiting C′-type shear bands indicating top-S shear; qtz, quartz; bt, biotite; plane light. (E) Staurolite-zone schist containing garnet porphyroblasts exhibiting asymmetric tails indicating top-S sense of shear; ms, muscovite; plane light. (F) Sillimanite-zone schist exhibiting C′-type shear bands indicating top-S sense of shear; sill, sillimanite; plane light. (G) Undulatory extinction in feldspar, suggesting deformation at >450 °C, in a garnet-zone orthogneiss; cross polars. (H) Grain-boundary migration, indicating temperatures >500 °C, in a kyanite-zone quartzite; cross polars. (I) Myrmekite (myrm) and incipient chessboard extinction in quartz, suggesting temperatures >600 °C and potentially >700 °C, in sillimanite-zone orthogneiss; cross polars.

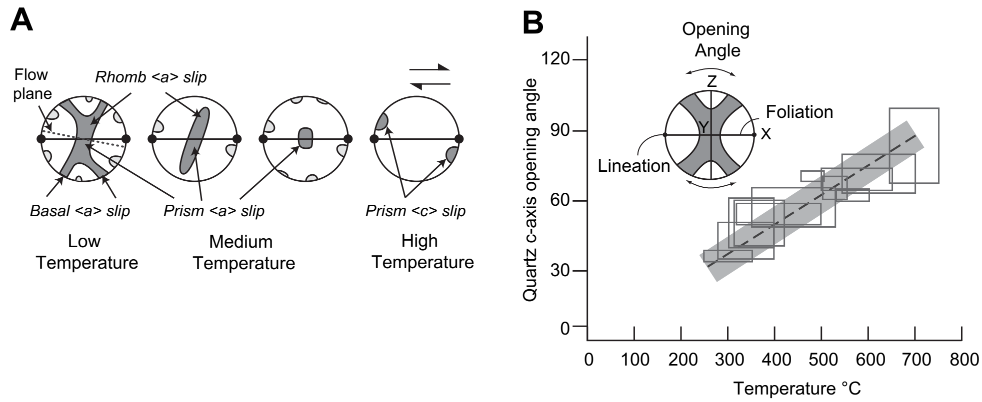

Fig. 7. Quartz lattice-preferred orientations (LPO) and associated temperature indicators. (A) Simplified stereonets showing dependence of quartz LPOs and inferred slip systems on increasing temperature. [c] axes are shown in dark gray and <a> axes in light gray. Modified from Passchier and Trouw (2005). (B) Relationship between [c] axis opening angle to temperature. Dashed line is the best fit line with ±50 °C error shown in gray. *X*, *Y*, and *Z* strain axes are shown. Data (boxes) from Kruhl (1998), Law et al. (1992), Nyman et al. (1995), and Okudaira et al. (1995). Modified from Law et al. (2004).

U/Pb zircon geochronology, and $^{40}Ar/^{39}Ar$ and apatite fission-track thermochronology indicate that D2 vertical thinning and horizontal extension, migmatization, and peak metamorphism began at 35.0 ± 0.8 Ma, was ongoing at 23.1 ± 0.8 Ma, and had ceased by 16.2 ± 0.4 Ma, a duration of 12–19 m.y. (Lee et al., 2006; Lee and Whitehouse, 2007). In Mabja Dome, metamorphic isograds, the S2 foliation, and mica $^{40}Ar/^{39}Ar$ chrontours are domed, but low-temperature potassium feldspar $^{40}Ar/^{39}Ar$ and apatite fission-track chrontours are not. Therefore, doming occurred at temperatures between ~400 °C (estimated blocking temperature for muscovite) and ~200 °C (estimated blocking temperature for the low-temperature steps in potassium feldspar) during the middle Miocene (Lee et al., 2006).

South of the North Himalayan gneiss domes, the GHS (Fig. 1) is characterized by exhumed middle crust with structural, metamorphic, anatectic, and intrusive histories similar to those recorded in Mabja Dome (e.g. Murphy and Harrison, 1999; Vance and Harris, 1999; Walker et al., 1999; Simpson et al., 2000; Searle et al., 2003). These similarities led Lee and Whitehouse (2007) to postulate that between late Eocene/early Oligocene to middle Miocene, this mid-crustal sequence was continuous from beneath southern Tibet southward to the high Himalaya. Furthermore, Lee et al. (2000, 2006) argued that to maintain strain compatibility, D2 ductile flow in the North Himalayan gneiss domes was accommodated at shallow crustal levels to the south by normal-sense (top to north) slip along the STDS. Lee and Whitehouse (2007) hypothesized that the combination of a continuous mid-crustal sequence, strain-compatibility arguments, and the interpretation that no net extension exists across the STDS (e.g., Searle et al., 2003) required that mid-crustal D2 ductile flow in southern Tibet was accommodated by southward channel flow and extrusion (e.g., Nelson et al. 1996; Hodges et al., 2001; Beaumont et al., 2001, 2004) since the late Eocene/early Oligocene. The kinematic, microstructural, and vorticity results we describe in this paper test this hypothesis.

3. Kinematics, deformation temperatures, and vorticity

To characterize patterns of ductile deformation in the exhumed mid-crustal rocks of Mabja Dome, microstructural analyses on 40 samples and quartz lattice-preferred orientation (LPO) analyses on 11 samples were completed to document shear sense and deformation temperatures. Diffraction patterns were collected using a JEOL 6300 scanning electron microscope coupled with an HKL Nordlys 2 EBSD camera. CHANNEL 5 HKL software was used to index the patterns with Hough resolution of 80, detecting 7–8 bands with standard divergence and a quartz structure file containing 60 reflectors. In addition, vorticity analyses on 28 samples were completed to document the spatial distribution of pure shear vs. simple shear. Samples were analyzed from the Triassic siliciclastic sequence (unit Ts), Paleozoic schist, quartzite, and orthogneiss units (units Pq, Pus, Pls, and Pop), and from the basal migmatitic orthogneiss (unit EOg), spanning the metamorphic sequence from chloritoid-zone to sillimanite-zone rocks (Figs. 4 and 5).

3.1. Kinematics

The spatial distribution of shear sense was determined using the asymmetry of strain shadows on metamorphic porphyroclasts (Fig. 6A, B, and E), inclusion patterns within metamorphic porphyroclasts (Fig. 6C), and C′-type shear bands (Fig. 6D and F) in oriented samples cut parallel to the L2 lineation and perpendicular to the S2 foliation. Electron backscatter diffraction (EBSD) was used to generate quartz LPOs, from which the asymmetry of the [c] and <a> axes patterns with respect to the foliation and lineation were used to determine shear sense (Fig. 7A) (e.g. Lister and Hobbs, 1980; Law, 1990).

In chloritoid-zone rocks, observed microstructural shear sense indicators such as σ-type strain shadows on chloritoid and iron-oxide porphyroclasts, inclusion patterns within chloritoid and iron-oxide porphyroclasts, and C′-type shear bands, show both top-N and top-S shear at the thin-section scale (Figs. 5 and 6A; Table 1). Several samples exhibited a greater number of top-N kinematic indicators, suggesting that top-N shear was locally dominant. Elsewhere, samples exhibited similar amounts of top-N and top-S shear sense indicators, implying that locally bulk pure shear dominated. Overprinting or cross-cutting top-N and top-S shear microstructures were not observed, suggesting that shear in both directions occurred simultaneously. Quartz LPO patterns within this zone are moderate to poor, but suggest top-S sense of shear in one sample and top-N in another (Fig. 8).

In garnet-zone rocks, microstructural shear sense indicators include σ-type strain shadows on chloritoid, garnet (Fig. 6B), and iron-oxide porphyroclasts, rotated internal foliation within garnet porphyroclasts (Fig. 6C), and C′-type shear bands. These microstructures change downward through the Ts unit from mixed top-N and top-S shear at higher structural levels (Fig. 6B) through top-N shear (Fig. 6C), and then dominantly top-S shear at deepest structural

Table 1
Summary of shear sense, vorticity, and temperature data.

Sample	Rock type	Shear sense	Vorticity (W_m)	% Pure shear	Deformation temperature (°C)	Metamorphic temperature (°C)	Temperature indicator[c]
A-A'-A″ Transect							
ctd-in							
MDP25a[a]	sch	t-N,[d] t-N[b]	0.80–0.82	40–38	~450–550	–	m.a.
MDP25b[a]	sch	t-N, t-S[e]; t-S[b]	–	–	~450–550	–	m.a.
MDP27	arg	t-N, t-S[e]	–	–	~450–550	–	m.a.
MDP28	arg	t-N[d]	0.75–0.78	44–42	~450–550	–	m.a.
gar-in							
MD25	sch	t-N[d]	0.80–0.82	40–38	~450–550	–	m.a.
MD27	sch	t-N, t-S[e]	–	–	~450–550	–	m.a.
MD28[a]	qtz	t-N[b]	–	–	375–475	–	o.a.; q.t.
MD32	sch	t-N	0.72–0.75	49–44	~450–550	–	m.a.
MD31a	sch	t-N	0.72–0.75	49–44	–	626 ± 55	Lee et al., 2004
MD29	sch	t-S	–	–	–	575 ± 50	Lee et al., 2004
MDP37	sch	t-S	0.77–0.84	43–37	–	–	–
MD34[a]	orth	t-S[b]	–	–	325–525	–	q.t.
MD36[a]	qtz	t-S, t-S[b]	–	–	450–625	–	q.t.
MDP45[a]	orth	t-S, t-S[b]	0.74–0.78	45–42	250–525	–	q.t.
MD38[a]	orth	t-N	0.73–0.75	48–44	450–775	–	q.t.
ky-in							
MDP52a[a]	qtz	t-S[b]	–	–	500–700	–	o.a.; q.t.
MDP52d	sch	t-S	0.62–0.69	56–51	–	–	–
MD40[a]	qtz	t-S, t-S[b]	–	–	–	–	–
stt-in							
MD42	sch	t-S	–	–	–	635 ± 58	Lee et al., 2004
MD44	sch	t-S	0.62–0.67	56–53	–	–	–
MDP56a	amph	t-S	0.55–0.68	62–52	–	–	–
sill-in							
MD51a	sch	–	–	–	–	~675	Lee et al., 2004
MDP65	sch	t-S	0.57–0.67	60–53	>600	–	m.a.
MD53	sch	t-S	–	–	>600	705 ± 65	Lee et al., 2004
MD55	sch	t-S	0.60–0.68	58–52	>600	–	m.a.
MD58	orth	t-S	0.52–0.68	63–52	–	–	–
MDP68[a]	orth	–	0.52–0.6	63–58	~700	–	q.t.
MDP69[a]	orth	–	–	–	~700	–	q.t.
B′-B″ Transect							
gar-in							
MD73	qtz	–	–	–	>450	–	f.t.
MD74a	sch	t-S	0.43–0.51	71–64	~450–550	–	m.a.
MD74b	sch	t-N	–	–	~450–550	–	m.a.
MD75	sch	t-S	0.33–0.58	77–59	~450–550	–	m.a.
MD76	sch	t-S	0.74–0.78	45–42	~450–550	–	m.a.
MD77	sch	–	0.42–0.50	72–65	>450	–	f.t.
MD93	pgn	–	0.55–0.60	62–58	~450–550	–	m.a.
MD94	sch	t-S	0.58–0.62	59–56	~450–550	–	m.a.
MD78	qtz	–	–	–	>450	–	f.t.
C-C′ Transect							
gar-in							
MD84	sch	t-N[d]	0.77–0.81	43–39	~450–550	–	m.a.
MD83	sch	t-N[d]	–	–	~450–550	–	m.a.
MD82	sch	t-N, t-S[e]	–	–	~450–550	–	m.a.
Transect D-D′							
gar-in							
MD110	sch	t-S[d]	0.71–0.78	50–42	~450–550	–	m.a.
MD111	sch	t-S[d]	–	–	~450–550	–	m.a.
MD112	sch	t-N[d]	0.69–0.71	51–50	~450–550	–	m.a.
MD113	sch	t-N, t-S[e]	–	–	~450–550	–	m.a.

Abbreviations: amph, amphibolite; arg, argillite; orth, orthogneiss; pgn, paragneiss; qtz, quartzite; sch, schist; t-S, top-south; t-N, top-north. Samples are in order of increasing structural depth, except transect D-D′ where all samples are from the same structural level.
[a] Sample analyzed with EBSD.
[b] Shear sense determined from EBSD-generated quartz LPO data.
[c] f.t., Feldspar textures; m.a., mineral assemblage; o.a., opening angle; q.t., quartz textures.
[d] Top-N or top-S shear sense makes up >60% of shear sense indicators.
[e] Subequal amounts of top-N and top-S shear.

levels (Fig. 5; Table 1). Quartz LPOs within the garnet-zone are relatively strong, with [c] axes transitional from type-I cross-girdles to Y-axis maxima (Fig. 8). Some show [c] and <a> axes that are weakly asymmetrical (MD36 and MDP45) suggesting non-coaxial shear; the most asymmetric LPO (MD28) implies top-N shear. In detail, few of the LPOs are exactly coincident with the foliation or lineation, implying that the strain recorded by the quartz LPO and the strain recorded by the foliation and lineation are not the same.

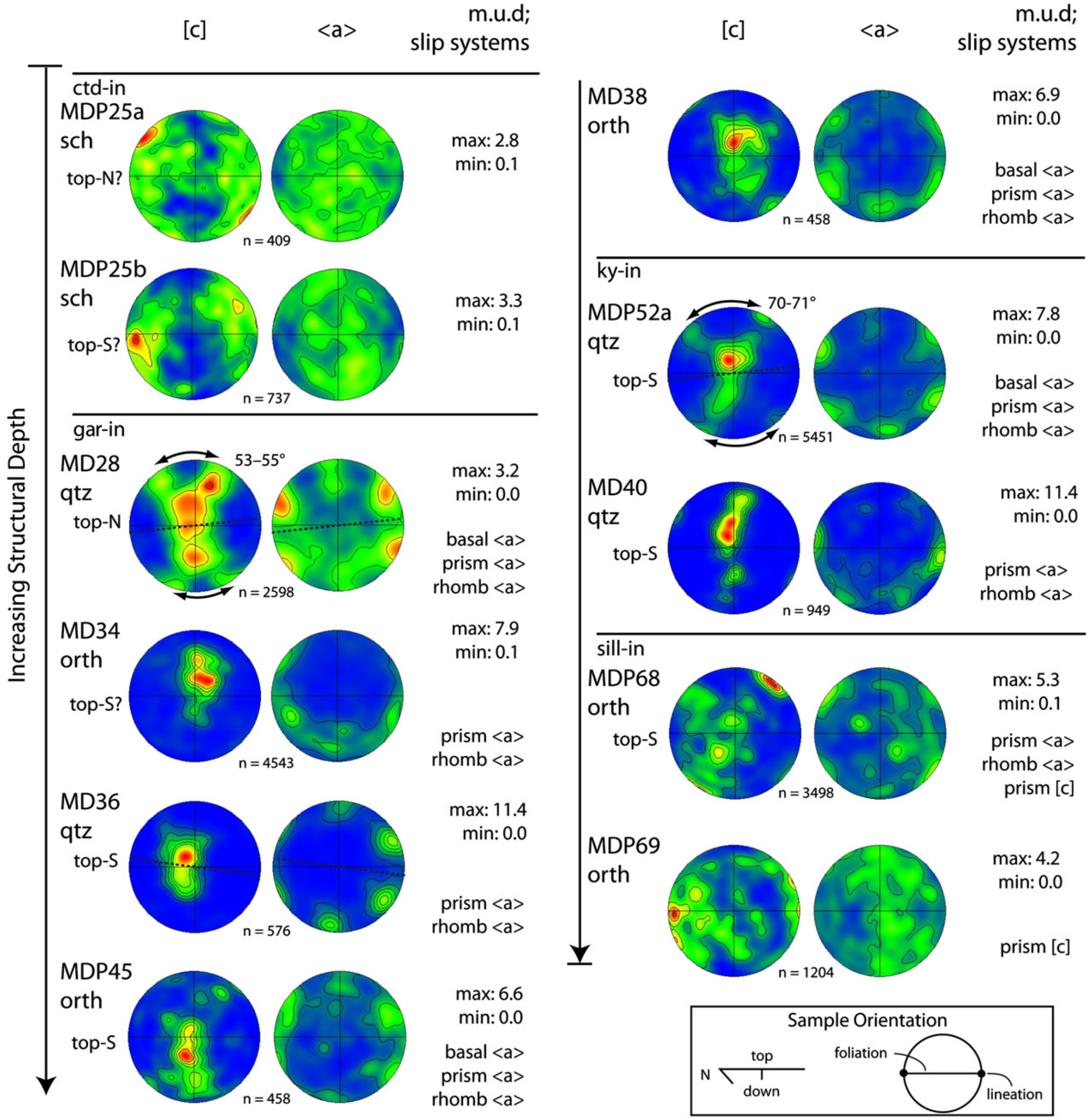

Fig. 8. EBSD-generated quartz LPOs from samples cut perpendicular to foliation and parallel to lineation along the A–A'–A″ transect (see Fig. 5). Upper hemisphere [c] and <a> axis stereonet plots shown. Metamorphic isograds, opening angle, shear sense, and number (n) of quartz grains measured noted. All plots oriented as indicated in the sample orientation box with the exception of MDP69 which has an unknown orientation. Data are point-per grain; contours are mean uniform density (m.u.d.) within indicated minimum (min) and maximum (max) values. Dashed line represents the flow plane. Sch, schist; qtz, quartzite; orth, orthogneiss.

In kyanite-zone and deeper rocks, microstructures such as σ-type strain shadows on garnet porphyroclasts (Fig. 6E), inclusion patterns within garnet porphyroclasts, and C′-type shear bands (Fig. 6D and E) show solely top-S shear (Fig. 5). Quartz LPOs from kyanite-zone samples are strong, with [c] axes transitional from type-I cross-girdles (MDP52a) to a single girdle (MD40), and have pronounced asymmetry suggesting top-S sense of shear (Fig. 8). The development of single girdles and type-I cross-girdles in this zone and structurally lower samples indicate plane strain (Lister and Hobbs, 1980). The quartz LPO from sillimanite-zone sample MDP68 is asymmetric with a [c] axis distribution suggesting top-S sense of shear. Sample MDP69 yields an asymmetric LPO of modest strength with [c] axis maxima subparallel to the X strain axis indicating prism [c] slip. However, this sample is not oriented so shear sense cannot be determined.

3.2. Deformation temperatures

Several techniques were used to estimate deformation temperature during the development of the kinematic and quartz LPO fabrics. Temperatures were estimated based on (1) mineral assemblages preserved within strain shadows of rotated porphyroclasts, (2) quartz and feldspar deformation microstructures (e.g. Jessell, 1987; Fitz Gerald and Stünitz, 1993; Lloyd and Freeman, 1994; Hirth et al., 2001; Stipp et al., 2002a,b), (3) quartz LPOs (e.g.

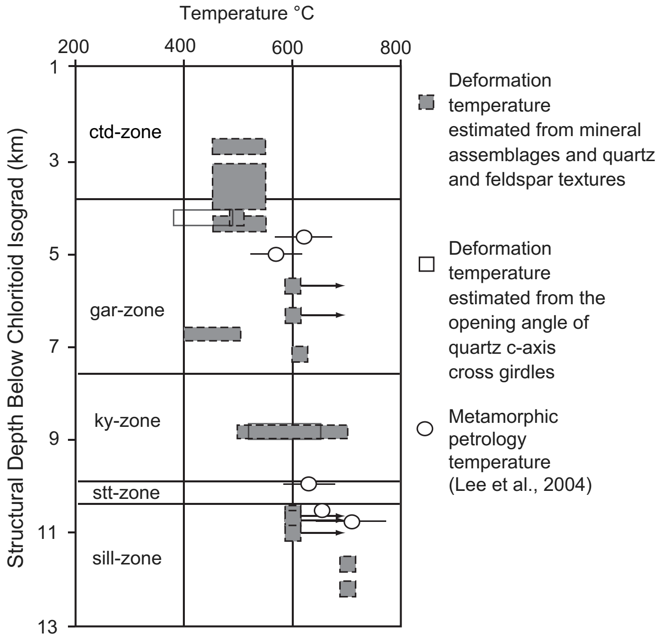

Fig. 9. Estimated deformation temperatures (boxes) for schists, orthogneisses, and quartzites compared to metamorphic petrology temperature estimates (circles with error bars) as a function of structural depth below the chloritoid-in isograd. Arrows indicate the estimate is a minimum. Ctd, chloritoid; gar, garnet; ky, kyanite; stt, staurolite; sill, sillimanite.

Mainprice et al., 1986; Tullis and Yund, 1992), and (4) the opening angle of quartz [c] axis LPOs (Kruhl, 1998; Law et al., 2004). For the latter, the opening angle is defined as the angle between the [c] axis girdles measured in the plane perpendicular to foliation and parallel to lineation (Fig. 7B) (Kruhl, 1998). Experimental (e.g. Tullis et al., 1973) and numerical simulation studies (e.g. Lister et al., 1978; Lister and Hobbs, 1980; Lister and Dornsiepen, 1982; Wenk et al., 1989) indicate that under some—but not all—circumstances, the opening angle of quartz [c] axis LPOs increases with increasing deformation temperature and hydrolytic weakening, and decreasing strain rate; other factors, such a strain path and strain geometry likely also play a role (Barth et al., in press). Deformation temperatures estimated from the quartz [c] axis opening angles overlap with deformation temperatures based on quartz and feldspar textures and mineral assemblages (Fig. 9), supporting our assumption that opening angle increases with increasing temperature.

Strain shadows on chloritoid, iron-oxide, and tourmaline porphyroclasts in chloritoid-zone pelites contain quartz + biotite + muscovite ± chlorite. This mineral assemblage suggests deformation temperatures of ~450–550 °C (Fig. 9; Table 1) (Spear and Menard, 1989). Quartz in the chloritoid-zone exhibits undulatory extinction, but no microfractures, indicating temperatures of at least ~350 °C (Hirth and Tullis, 1992; Stipp et al., 2002a).

Quartz + biotite + muscovite ± chlorite are present in the strain shadows around chloritoid, garnet, iron-oxide, tourmaline, and biotite porphyroclasts in garnet-zone pelites, suggesting deformation temperatures of ~450–550 °C (Fig. 9; Table 1) (Spear and Menard, 1989). Quartz exhibits a weak grain-shape foliation, deformation lamellae, undulose extinction, and regime 2 microstructures (Hirth and Tullis, 1992) indicating temperatures of at least ~500 °C (Stipp et al., 2002a,b). Feldspar exhibits undulatory extinction suggesting temperatures in excess of 450 °C (Fig. 6G) (Pryer, 1993). Quartz [c] axis LPOs suggest a transition with structural depth from basal <a>, through mixed <a>, to rhomb + prism <a> slip, indicating deformation temperatures between 400–500 °C toward the top and <650 °C toward the bottom of the garnet-zone (Figs. 7 and 8) (Mainprice et al., 1986). Finally, the opening angle of quartz LPO cross-girdles at the top of the garnet-zone suggest a deformation temperature of ~425 °C (Figs. 8 and 9; Table 1).

Strain shadows around garnet porphyroclasts within kyanite-zone pelites contain quartz + biotite + muscovite. Those in the sillimanite-zone contain quartz + biotite + muscovite ± sillimanite, suggesting deformation temperatures in excess of 600 °C. Quartz at these deepest structural levels exhibits regime 3 microstructures (Fig. 6H) (Hirth and Tullis, 1992), implying an increase in deformation temperature from ~500 °C to ~650 °C (Stipp et al., 2002a). Weakly developed chessboard extinction is present at the deepest structural levels, indicating temperatures in excess of 700 °C (Fig. 6I) (Mainprice et al., 1986; Stipp et al., 2002a). Feldspar exhibits myrmekite at the deepest structural levels, which also suggest temperatures of >600 °C (Fig. 6I) (Simpson, 1985). Quartz [c] axis LPOs within the kyanite-zone and deeper rocks suggest a transition with structural depth from mixed <a> slip to poorly developed prism [c] slip at the deepest structural levels (Fig. 8), suggesting deformation temperatures that increase from ~500 °C to >650 °C. The opening angle of the LPO from sample MDP52a, collected from the middle of the kyanite-zone, suggests a deformation temperature of 515–650 °C (Fig. 8).

3.3. Vorticity

To characterize the style of flow recorded in the strongly deformed, exhumed mid-crustal rocks of Mabja Dome, vorticity analyses were completed to document the relative percentage of pure and simple shear during ductile deformation. Characterizing vorticity is important because a large pure shear indicates significant vertical thinning and horizontal extension, and an increase in strain and extrusion rates relative to simple shear. Kinematic vorticity number (W_k) measures the relative contributions of pure ($W_k = 0$) and simple ($W_k = 1$) shear during steady-state (instantaneous) deformation, and pure and simple shear components are equal when $W_k = 0.71$ (Law et al., 2004). However, because the vorticity of flow varies both spatially and temporally in naturally deformed rocks (e.g. Fossen and Tikoff, 1997, 1998; Jiang, 1998), flow vorticity is better characterized by the mean kinematic vorticity number (W_m), which is the result of a time-averaged and an assumed steady-state deformation history. To estimate W_m, we applied the rigid-grain technique (Passchier, 1987; Wallis et al., 1993) to thin sections cut perpendicular to the S2 foliation and parallel to the L2 lineation. Measurements were made either directly from the thin section or from photomicrographs using the imaging software ImageJ (Rasband, 2005).

The rigid-grain technique (Wallis et al., 1993) entails measuring the aspect ratio (R) of a rigid porphyroclast such as garnet, chloritoid, and tourmaline and the acute angle (θ) between the clast long axis and the macroscopic foliation. Grains above a critical aspect ratio (R_c) will define a stable orientation, whereas grains below will rotate, showing a range of angles. From R_c, vorticity can be calculated as (Passchier, 1987):

$$W_m = \left(R_C^2 - 1\right)/\left(R_C^2 + 1\right) \tag{1}$$

Plotting the shape factor (B^*), where

$$B^* = \left(M_x^2 - M_n^2\right)/\left(M_x^2 + M_n^2\right) \tag{2}$$

and M_x = long axis and M_n = short axis of a clast, vs. θ on the Rigid-Grain Net is a graphical approach to calculating W_m (Fig. 10; Jessup

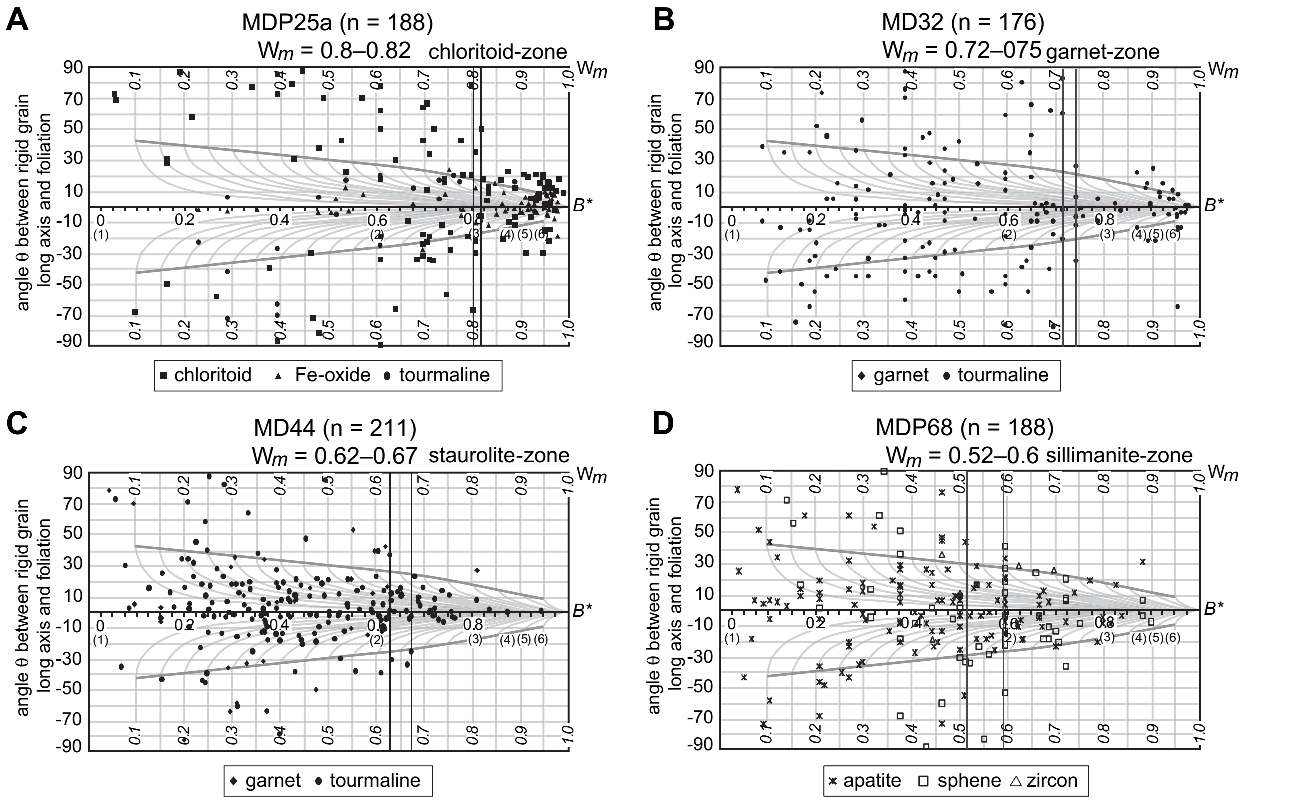

Fig. 10. Representative Rigid-Grain Net (RGN) plots[1] of shape factor, B^*, vs. the angle θ between the rigid-grain long axis and macroscopic foliation for an intermediate-structural depth chloritoid-zone phyllite (A), intermediate-depth garnet-zone schist (B), a structurally deep staurolite-zone schist (C), and a structurally deep sillimanite-zone orthogneiss (D). Mean vorticity, W_m, shown as pale gray curves; R values in parentheses; n = the number of data.

et al., 2007). Similar to R_c, the critical shape factor B_c^* separates grains that reached a stable orientation vs. those that rotated freely. B^* and W_m are scaled one to one, thus W_m can be determined directly from B^*.

To successfully apply the rigid-grain technique, the following criteria must be met: (1) the porphyroclasts must predate the dominant deformation fabric, (2) the porphyroclasts are internally undeformed, (3) there was no mechanical interaction between adjacent clasts or the matrix, and (4) the porphyroclasts are in a homogeneously deformed matrix. Uncertainties in vorticity values estimated using this technique can be attributed to: (1) recrystallization-induced changes in the aspect ratio (R) during or after deformation, (2) large-aspect ratio rigid grains in low-strain rocks may not have rotated into their stable orientations, and (3) fracturing of rigid grains with large-aspect ratios (Jessup et al., 2007). Rigid grains used to estimate vorticity in Mabja showed little to no recrystallization and rigid grains with large-aspect ratios were not fractured (Fig. 10).[1]

Mean vorticity estimates for schists and orthogneisses from two transects approximately parallel to the L2 stretching lineation, A–A′–A″ and C–C′, and one at a high angle to the lineation, D–D′ (Figs. 4 and 5), range from 0.75–0.82 (44–38% pure shear) within chloritoid-zone rocks (Figs. 10A and 11) to 0.69–0.84 (51–36% pure shear) within garnet-zone rocks (Figs. 10B and 11; Table 1). Samples from the chloritoid-zone and the uppermost part of the garnet-zone (unit Ts, Fig. 4) exhibit both top-N and top-S shear at the microscopic scale. Because of the opposing shear sense indicators, vorticity estimates from this unit are assumed to be reliable only if the sample was dominated (>60%) by one direction of shear. For those chloritoid-zone samples that exhibit subequal amounts of top-N and top-S shear, deformation locally was likely characterized by bulk pure shear. Schists and orthogneisses in garnet-zone rocks collected along a transect nearly perpendicular to the stretching lineation, B′–B″ (Figs. 4 and 5) record W_m from 0.33–0.62, indicating a significantly higher (77–56%) component of pure shear. The exception is sample MD76, which yields $W_m = 0.74–0.78$ (45–42% pure shear) (Table 1). Schist and orthogneiss W_m values decrease from 0.62–0.69 (56–51% pure shear) within the kyanite-zone rocks, to 0.52–0.68 (63–52% pure shear) within the staurolite- and sillimanite-zone rocks (Figs. 10C, D, and 11; Table 1). Contours of average percent pure shear recorded in schists and orthogneisses across the west-central portion of Mabja Dome show an increase in pure shear component with structural depth and toward the south (Fig. 12).

4. Discussion

Field and structural data from the Kangmar and Mabja domes, combined with strain-compatibility arguments, led Lee et al. (2000, 2006) to suggest that normal slip along the STDS merged with increasing depth into a zone of ductile shear that terminated in a mid-crustal zone of bulk coaxial strain that is now exposed in the cores of these domes. Lee et al. (2000, 2006) envisaged that within this mid-crustal coaxial strain zone, rheologically weakened middle crustal rocks were vertically thinned and horizontally stretched, resulting in the development of the subhorizontal D2 fabrics. However, our detailed microstructural kinematic indicator and

[1] Additional Rigid-Grain Net plots can be found in the Data Repository.

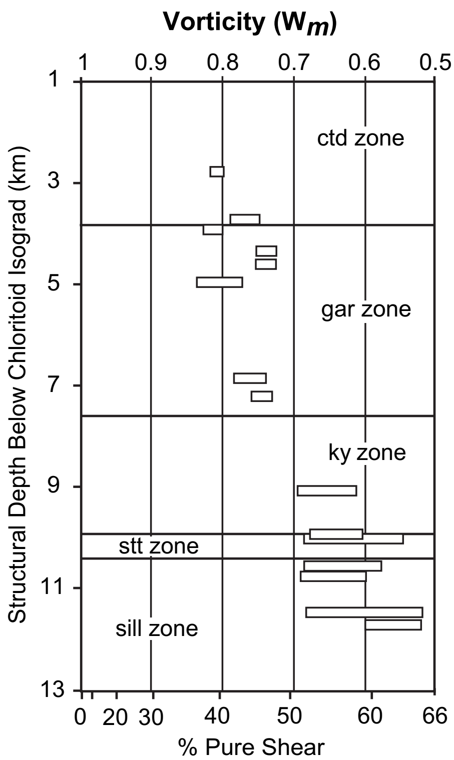

Fig. 11. Rigid-grain technique estimated vorticity and percent pure shear for schists and orthogneisses plotted as a function of structural depth below the chloritoid-in isograd along cross section A–A'–A″. Cross section location shown in Fig. 4.

quartz LPO data from Mabja Dome yield a different pattern of shear. Shear sense within Mabja varies with depth from a mix of top-S and top-N shear, with top-N shear slightly dominant, within chloritoid-zone rocks, through dominantly top-S shear within garnet- and kyanite-zone rocks, to solely top-S shear within the staurolite-zone and deeper rocks (Fig. 5; Table 1). This kinematic flow pattern contrasts with the dominantly top-N D2 ductile extensional deformation documented in several other North Himalayan gneiss domes, including Kangmar, Malashan, and Kampa domes (Chen et al., 1990; Aoya et al., 2005, 2006; Quigley et al., 2008; but see Lee et al., 2000) (Fig. 1). One possible explanation for the differences in flow patterns is that D2 deformation fabrics in Mabja Dome developed at a distinctly deeper structural level compared to the other domes (Kawakami et al., 2007).

The rigid-grain technique shows that schists and orthogneisses record general shear ($W_m = 0.33$–0.84, 77–36% pure shear) and an increase in pure shear with structural depth, ranging from an average of ~44% pure shear ($W_m = 0.75$) in chloritoid- and garnet-zone rocks to ~63% pure shear ($W_m = 0.52$) in kyanite-zone and deeper rocks. An increase in lithostatic pressure may explain the increase in pure shear component observed with increasing depth. The general pattern of increasing pure shear with depth is interrupted by chloritoid-zone rocks that locally record bulk pure shear.

Deformation temperatures associated with sense-of-shear fabrics and vorticity increase with structural depth from ~450 °C within chloritoid-zone rocks, to ~600 °C within garnet-zone rocks, to ~700 °C at the deepest structural levels within sillimanite-zone rocks, and define a ~34 °C/km deformation temperature field gradient (Fig. 9; Table 1). Deformation temperatures within rocks in the chloritoid-zone and the upper part of the garnet-zone may be cooler than peak metamorphic temperatures, whereas deformation temperatures for kyanite-zone and deeper rocks overlap with petrologically determined temperatures (Fig. 9) (Lee et al., 2004). These relations imply that the kinematic fabrics and vorticity were recorded after peak metamorphic temperatures at moderate structural depths, and at peak metamorphic conditions at deep structural levels, consistent with textural relations that show peak metamorphism was pre- to syn-D2 deformation (Lee et al., 2004).

The overlap of estimated deformation temperatures with quantitative metamorphic temperatures at deeper structural depth indicates that the kinematics and vorticity of D2 ductile flow was synchronous with peak metamorphism and migmatization. Thus, the cooling history defined by U/Pb zircon and $^{40}Ar/^{39}Ar$ mica ages that bracket metamorphism and migmatization also bracket D2 kinematic fabrics and vorticity between initiation at 35.0 ± 0.8 Ma and cessation by ~18.3 Ma (Fig. 13) (Lee et al., 2006; Lee and Whitehouse, 2007).

An increase in pure shear component with depth indicates a significant change in vertical thinning and horizontal extension as a function of depth, consistent with the observed subhorizontal D2 foliation and stretching lineation, and, relative to simple shear, an increase in strain and extrusion rates (e.g. Pfiffner and Ramsay, 1982; Ramsay and Huber, 1987). We combine an estimated 50–10% (X/Z ratio $= R_{xz} \geq 4$) vertical thinning of chloritoid-zone rocks (Lee et al., 2004) and plane strain, indicated by the well-defined LS-tectonites (Lee et al., 2004) and our quartz LPO patterns, with our vorticity data (W_m), to place crude constraints on the magnitude of stretch (S^{-1}) parallel to the flow plane (Wallis et al., 1993):

$$S = \left\{ 0.5\left(1 - W_m^2\right)^{0.5} \left[\left(R_{xz} + R_{xz}^{-1} + \frac{2\left(1 + W_m^2\right)}{\left(1 - W_m^2\right)} \right)^{0.5} + \left(R_{xz} + R_{xz}^{-1} - 2 \right)^{0.5} \right] \right\}^{-1} \tag{3}$$

R_{xz} (Lee et al., 2004) and our W_m values yield stretches of ~34–38% parallel to the flow-plane transport direction. Compared to chloritoid-zone rocks, garnet-zone and deeper rocks exhibit greater strains, and kyanite-zone and deeper rocks record greater pure shear components, implying that these rocks record a larger percentage of stretch parallel to the flow direction. The GHS exposed on the Everest massif also records a significant component of pure shear (36–53%) (Law et al., 2004; Jessup et al., 2006). These observations, combined with finite-strain data, suggest a sub-horizontal stretch of at least 10–40% within the GHS (Law et al., 2004).

If Asia acted as a lithostatic backstop, strain compatibility and a horizontal stretch of 10–38% in the middle crust of southern Tibet and the high Himalaya require that the vertical thinning and horizontal stretching deformation was accommodated by southward flow and extrusion of the middle crust (Fig. 14). One of the consequences of this interpretation is that heterogeneous pure shear across the middle crust will induce shear strains that vary as a function of both distance from Asia and of the pure shear gradient perpendicular to the mid-crustal boundaries (e.g. Ramsay and Huber, 1987; Vannay and Grasemann, 2001). These relationships, in turn, predict an increase in displacement from north to south across the MCT and STDS (Fig. 14). In this interpretation, the transect from the GHS exposed in the Everest region to the high-grade metasedimentary rocks exposed in Mabja defines an ~140 km-long mid-crustal channel from its extruding edge (e.g. Grujic et al., 1996; Beaumont et al., 2001; Hodges et al., 2001) to closer to its ductile source. Finally, although a significant component of pure shear indicates vertical thinning and subhorizontal extension, this

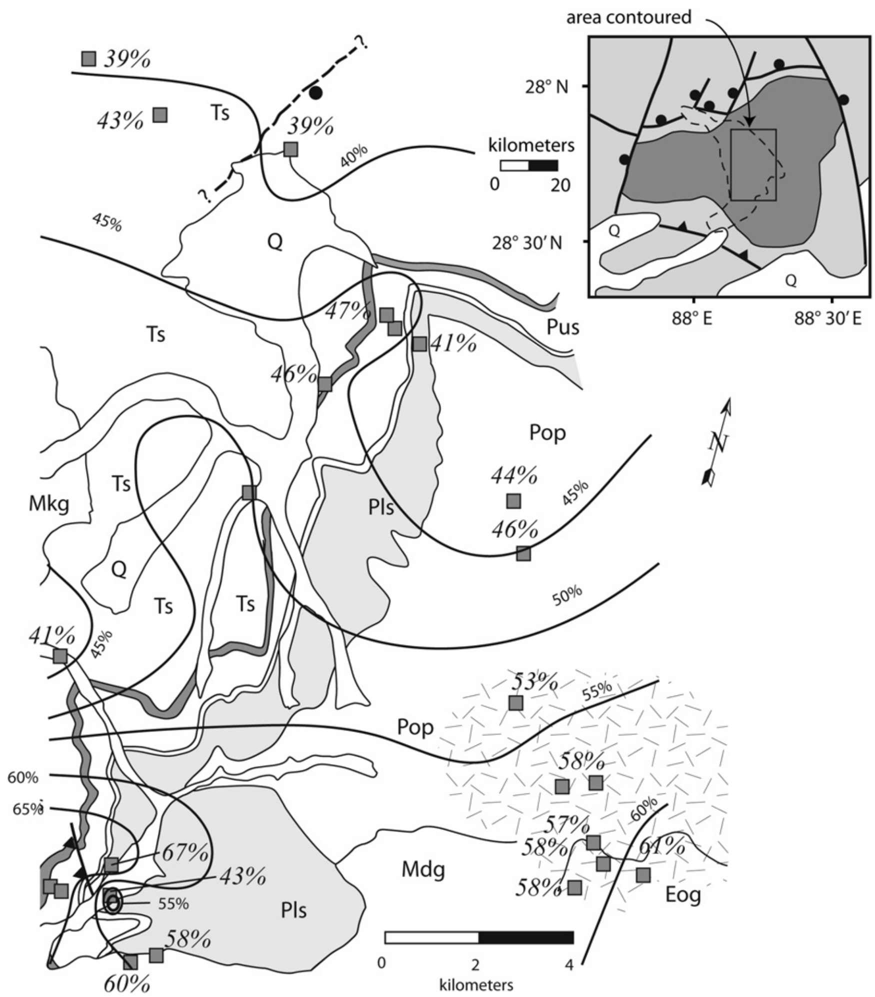

Fig. 12. Contour map of average percent pure shear estimated using the rigid-grain technique for schists and orthogneisses across a portion of Mabja Dome. Contours interpolated from sample locations and W_m estimates using ArcGIS (ESRI, 2005). Contour interval is 5%. Average percent pure shear for each sample in italics. Sample number and map explanation shown in Figs. 4 and 5. Inset map shows location of contoured area.

part of the Himalayan–Tibetan crust could have maintained or increased its thickness by underplating of new material (Law et al., 2004).

The patterns of ductile flow preserved in the mid-crustal rocks exhumed in the core of Mabja Dome are characterized by mixed top-N and top-S shear, with top-N shear slightly dominant, and ~44% pure shear at moderate structural levels; dominantly top-S shear and ~51% pure shear at deeper structural levels; and solely top-S shear and ~63% pure shear at the deepest structural levels. These patterns define mid-crustal ductile flow that is non-ideal compared to patterns predicted by channel-flow models (Figs. 2 and 3). Two different mechanisms may explain the near-equal mix of top-N and top-S shear at the top of the channel. First, reverse flow can be driven by either a variation in flow velocity as a result of heterogeneity in viscosity and will lead to a mix of top-N and top-S shear within chloritoid-zone rocks (Fig. 5). Second, reverse flow can be a result of a pressure difference along the length of the channel as a result of spatially varying channel thickness (Mancktelow, 1995; Grujic, 2006). In Mabja Dome rocks, the former may explain the observed top-N and top-S shear in chloritoid-bearing rocks. These rocks are composed, in large part, of graphite-bearing schists. Graphite is weak, and might localize strain. However, studies on graphitic schists in the Alps show that if fluids are present during deformation, graphite can be brittle at conditions where it is expected to be ductile

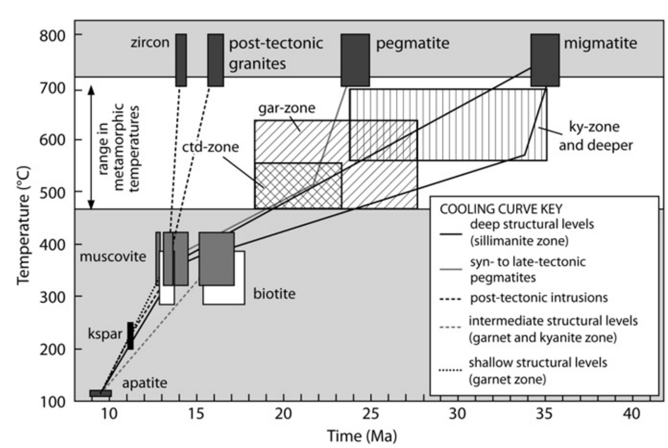

Fig. 13. Deformation temperatures for chloritoid-, garnet-, and kyanite-zone and deeper rocks superimposed on cooling histories for deformed migmatites, schists, orthogneisses, pegmatites and undeformed granites in Mabja Dome. Zircon U/Pb ages, mica and potassium feldspar 40Ar/39Ar ages, and apatite fission track ages from Lee et al. (2006) and Lee and Whitehouse (2007). Range in quantitative metamorphic temperatures (Lee et al., 2004) shown. Modified from Lee et al. (2006).

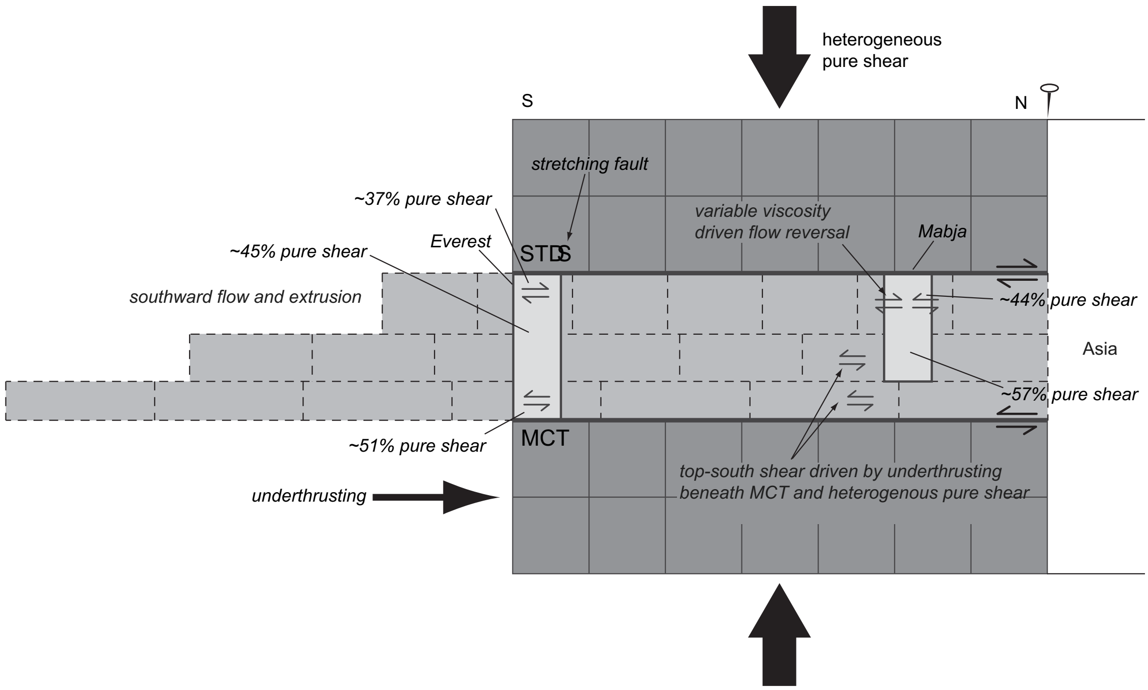

Fig. 14. Schematic diagram of heterogeneous pure shear-driven southward ductile flow and extrusion of middle crustal rocks (light gray) between the STDS and the MCT in southern Tibet and the high Himalaya. Dashed rectangles in the middle crust are schematic strain markers (compare to the solid squares above and below the middle crust). Arrow pairs indicate sense of shear. Pale gray boxes show relative locations of the GHS exposed in the Everest massif and rocks exposed in Mabja Dome. Percent pure shear values are from Law et al. (2004), Jessup et al. (2006), and this work. Dark gray boxes in the hanging wall of the STDS and the footwall of the MCT are shown as rigid. See text for discussion.

(Selverstone, 2005). Heterogeneous fluid content throughout the graphitic schists could have generated zones of varying viscosity, yielding opposing shear sense at the microstructural scale. Alternatively, the observed near-equal mix of top-N and top-S shear may be explained by local bulk pure shear.

The dominant top-S shear at deeper structural levels may be explained by the bottom half of the parabolic velocity field defined by Poiseuille flow due to a horizontal gradient in lithostatic pressure (Figs. 2 and 3), a large component of Couette flow due to underthrusting beneath the MCT (Figs. 2 and 3), and/or extrusion of middle crust as a consequence of the pure shear component of flow (Fig. 14). Four factors can influence the style of channel flow, assuming a crust of uniform density and a parallel-sided channel: (1) viscosity within the channel, (2) the velocity of the bounding plates, (3) the thickness of the channel, and (4) the pressure gradient along the channel (Turcotte and Schubert, 2002). A decrease in viscosity within the channel, a decrease in relative plate velocity, an increase in channel thickness, and/or an increase in pressure gradient lead to an increase in Poiseuille flow; the opposites favor Couette flow. Poiseuille flow could have been favored by the generation of low-viscosity migmatites within Mabja Dome and the constant velocity between the bounding plates since collision between India and Asia at ∼50–55 Ma (e.g. DeCelles et al., 2002; Guillot et al., 2003; Leech et al., 2005). Couette flow, however, could have been promoted by: (1) thinning of the channel, as indicated by the significant component of pure shear deformation recorded in Mabja (Fig. 14); (2) a small difference in horizontal gravitational potential-energy gradient between the Tibetan Plateau and its margins because of the potential lack of significant relief or crustal thickness during the early stages of D2 deformation (late Eocene to early Oligocene) (e.g. Molnar et al., 1993, but see Rowley and Currie, 2006); and/or (3) slow erosion rates until the early Miocene (e.g. Guillot et al., 2003). If this interpretation is correct, it implies that top-S shear was driven, in part, by underthrusting in the footwall of the MCT and that the MCT is present beneath the deepest exposures mapped in Mabja Dome. Our data, however, do not allow us to calculate the relative contributions of Poiseuille vs. Couette flow to the development of this hybrid flow regime at the deepest structural levels in Mabja Dome (Fig. 3b).

The structural, metamorphic, anatectic, and intrusive histories recorded in the North Himalayan gneiss domes are similar to those in the GHS (cf. Murphy and Harrison, 1999; Vance and Harris, 1999; Walker et al., 1999; Simpson et al., 2000; Searle et al., 2003; Lee et al., 2006; Lee and Whitehouse, 2007; Quigley et al., 2008). These similarities suggest that from late Eocene/early Oligocene to middle Miocene, high-grade mid-crustal metasedimentary and orthogneissic rocks, cut by anatectic melts and leucogranites, were continuous from beneath southern Tibet southward to the high Himalaya. The geologic histories in the metamorphic cores of the gneiss domes and the GHS are broadly similar (cf. Searle et al., 2003; Lee and Whitehouse, 2007), however vorticity and deformation temperature data from mid-crustal rocks in Mabja Dome differ somewhat from similar data collected from mid-crustal rocks of the GHS exposed in the Everest Massif region (Law et al., 2004; Jessup et al., 2006), ∼140 km southwest of Mabja Dome (Fig. 1), and from the base of the GHS in the Sutlej Valley (Grasemann et al., 1999), ∼1100 km west-northwest of Mabja Dome. In the Everest region, kinematic and vorticity studies showed that high-grade, structurally deep rocks at the top of the GHS record general shear (48–41% pure shear) with top-N sense of shear at close to peak metamorphic conditions, whereas lower-grade, structurally higher rocks record sub-simple shear (38–36% pure shear) with a well-developed top-N sense of shear at somewhat lower temperatures (Law et al., 2004; Jessup et al., 2006). At the base of the GHS, just above the MCT, the rocks record the highest pure shear component (53–48% pure shear) and top-S shear. These data led Jessup et al. (2006) to conclude that flow was spatially and temporally partitioned—high-temperature samples recorded the early stages of channel flow/extrusion at middle crustal depths and structurally higher, lower temperature samples recorded sub-simple shear flow at the upper margin of the channel during later stages of exhumation. Jessup et al. (2006) postulated that the pure shear component observed in rocks just above the MCT was the result of an increase in lithostatic load toward the base of the GHS. In the Sutlej River, Grasemann et al. (1999) showed that GHS orthogneiss mylonites within the MCT zone recorded vorticity values close to top-S simple shear for earlier high-temperature deformation and an increasing component of pure shear for later, low-temperature deformation. In contrast to the Jessup et al. (2006) interpretation, Grasemann et al. (1999) suggested that their vorticity data indicated that the flow regime was temporally partitioned following a decelerating strain path. These comparisons suggest that patterns of middle crustal flow in southern Tibet and the high Himalaya varied spatially, temporally, and rheologically.

5. Conclusions

New detailed microscopic kinematic analyses, deformation-temperature estimates, and vorticity analyses within mid-crustal rocks from Mabja Dome show a downward progression from mixed top-N and top-S shear in chloritoid-zone rocks, through dominantly top-S shear in garnet- and kyanite-zone rocks, to solely top-S shear in staurolite-zone and deeper rocks. The schists and orthogneisses record general shear deformation ($W_m = 0.33$–0.84, 77–36% pure shear) with an increasing component of pure shear with structural depth. A combination of mineral assemblages, microstructures, and quartz LPOs indicate that deformation temperatures ranged from $\sim$450 °C in chloritoid-zone rocks to $\sim$700 °C in sillimanite-zone rocks. Deformation temperatures in rocks of the chloritoid-zone and the upper part of the garnet-zone are somewhat lower than metamorphic petrology peak temperature estimates, whereas deformation temperatures for deeper rocks overlap with petrologically determined temperatures. These data indicate that the vorticity recorded in these rocks corresponds to the period of post- to syn-peak metamorphism, implying that these fabrics formed in the middle crust between $\sim$35 and $\sim$18 Ma. The large component of pure shear deformation recorded in these mid-crustal rocks indicates significant vertical thinning and horizontal stretching parallel to the flow-plane transport direction. Strain compatibility and horizontal stretch parallel to the flow-plane transport direction requires that middle crustal ductile deformation in southern Tibet was accommodated by southward flow and extrusion. Patterns of mid-crustal ductile flow in the Mabja area define a hybrid flow regime that is more complex than predicted by channel-flow models and involved: (1) locally a subequal mix of top-N and top-S shear at the highest structural levels that reflects either spatial variations in viscosity and/or bulk pure shear, (2) an increase in pure shear component with depth, the result of an increase in lithostatic load, and (3) solely top-S shear at the deepest structural levels, the result of mixed Couette and Poiseuille flow.

Acknowledgments

We thank R. Law, M. Jessup, and S. Wallis for discussions about vorticity analyses, R. Law and M. Jessup for discussions about their work on the Everest massif, and R. Jamieson for discussions on the processes driving middle crustal flow. Thanks also to W. Sullivan, K. Larson, and B. Dunne whose reviews helped strengthen a previous version of this manuscript. This research was supported by grants from the Geological Society of America, Central Washington University, and Sigma Xi awarded to J. Langille. Support was also provided by NSF grants EAR-0838146 awarded to J. Lee and EAR-0838264 awarded to B. Hacker.

Appendix. Supplementary data

Supplementary data associated with this article can be found, in the online version, at doi:10.1016/j.jsg.2009.08.009.

References

Aoya, M., Wallis, S.R., Terada, K., Lee, J., Kawakami, T., Wang, Y., Heizler, M., 2005. North-south extension in the Tibetan crust triggered by granite emplacement. Geology 33, 853–856.
Aoya, M., Wallis, S.R., Kawakami, T., Lee, J., Wang, Y., Maeda, H., 2006. The Malashan gneiss dome in south Tibet: comparative study with the Kangmar dome with special reference to kinematics of deformation and origin of associated granites. In: Law, R.D., Searle, M.P., Godin, L. (Eds.), Channel Flow, Ductile Extrusion and Exhumation in Continental Collision Zones. Geological Society, London Special Publications, vol. 268, pp. 471–495.
Armijo, R., Tapponnier, P., Mercier, J., Han, T., 1986. Quaternary extension in southern Tibet: field observations and tectonic implications. Journal of Geophysical Research 91, 13803–13872.
Barth, N.C., Hacker, B.R., Seward, G.G.E., Walsh, E.O., Young, D., Johnston, S. Strain within the ultrahigh-pressure Western Gneiss region of Norway recorded by quartz CPOs. In: Geological Society, London, Special Publications, in press.
Beaumont, C., Jamieson, R.A., Nguyen, M.H., Lee, B., 2001. Himalayan tectonics explained by extrusion of a low-viscosity crustal channel coupled to focused surface denudation. Nature 414, 738–742.
Beaumont, C., Jamieson, R.A., Nguyen, M.H., Medvedev, S., 2004. Crustal channel flows: 1. Numerical models with applications to the tectonics of the Himalayan–Tibetan orogen. Journal of Geophysical Research 109, 1–29.
Beaumont, C., Nguyn, M.H., Jamieson, R.A., Ellis, S., 2006. Crustal flow modes in large hot orogens. In: Law, R.D., Searle, M.P., Godin, L. (Eds.), Channel Flow, Ductile Extrusion and Exhumation in Continental Collision Zones. Geological Society, London, Special Publications, vol. 268, pp. 91–145.
Brookfiel, M.E., 1993. The Himalayan passive margin from Precambrian to Cretaceous. Sedimentary Geology 84, 1–35.
Burbank, D.W., Beck, R.A., Mulder, T., 1996. The Himalayan foreland basin. In: Yin, A., Harrison, T.M. (Eds.), The Tectonic Evolution of Asia. Cambridge University Press, New York, pp. 149–188.
Burg, J.P., Brunel, M., Gapais, D., Chen, G.M., Liu, G.H., 1984. Deformation of leucogranites of the crystalline Main Central sheet in southern Tibet (China). Journal of Structural Geology 6, 535–542.
Burg, J.P., Chen, J.M., 1984. Tectonics and structural zonation of southern Tibet, China. Nature 311, 219–223.
Burg, J.P., Leyreloup, A., Girardeau, J., Chen, G.M., 1987. Structure and metamorphism of a tectonically thickened continental crust: the Yalu Tsangpo suture zone (Tibet). In: Royal Society of London Philosophical Transactions A, vol. 321 67–86.
Chen, Z., Liu, Y., Hodges, K.V., Burchfield, B.C., Royden, L.H., Deng, C., 1990. The Kangmar Dome: a metamorphic core complex in southern Xizang (Tibet). Science 250, 1552–1556.
DeCelles, P.G., Robinson, D.M., Zandt, G., 2002. Implications of shortening in the Himalayan fold-thrust belt for uplift of the Tibetan plateau. Tectonics 21, 1–25.
Dewane, T.J., Stockli, D.F., Hager, C., Taylor, M., Ding, L., Lee, J., 2006. Timing of Cenozoic E–W extension in Tangra Yum Co rift, central Tibet. Journal of Asian Earth Sciences 26, 133.
Environmental Systems Research Institute, 2005. ArcMap 9.1, [Computer Software]. Environmental Systems Research Institute, Redlands, CA.
Fielding, E.J., Isacks, B.L., Barazangi, M., Duncan, C., 1994. How flat is Tibet? Geology 22, 163–167.
Fitz Gerald, J.D., Stünitz, H., 1993. Deformation of granitoids at low metamorphic grades. I: reactions and grain size reduction. Tectonophysics 221, 269–297.
Fossen, H., Tikoff, B., 1997. Forward modeling of non-steady-state deformations and the 'minimum strain path'. Journal of Structural Geology 19, 987–996.
Fossen, H., Tikoff, B., 1998. Forward modeling of non-steady-state deformations and the 'minimum strain path': reply. Journal of Structural Geology 20, 979–981.
Gaetani, M., Garzanti, E., 1991. Multicyclic history of the northern India continental margin (northwestern Himalaya). American Association of Petroleum of Geologists Bulletin 75, 1427–1446.
Gansser, A., 1964. Geology of the Himalayas. Wiley-Interscience, London.
Garzanti, E., 1999. Stratigraphy and sedimentary history of the Nepal Tethys Himalaya passive margin. Journal of Asian Earth Sciences 17, 805–827.
Godin, L., Grujic, D., Law, R.D., Searle, M.P., 2006. Channel flow, ductile extrusion and exhumation in continental collision zones; an introduction. In: Law, R.D., Searle, M.P., Godin, L. (Eds.), Channel Flow, Ductile Extrusion and Exhumation in Continental Collision Zones. Geological Society, London, Special Publications, vol. 268, pp. 1–23.
Grasemann, B., Fritz, H., Vannay, J.-C., 1999. Quantitative kinematic flow analysis from the Main Central Thrust Zone (NW-Himalaya, India): implications for

a decelerating strain path and the extrusion of orogenic wedges. Journal of Structural Geology 21, 837–853.

Grujic, D., 2006. Channel flow and continental collision tectonics: an overview. In: Law, R.D., Searle, M.P., Godin, L. (Eds.), Channel Flow, Ductile Extrusion and Exhumation in Continental Collision Zones. Geological Society, London, Special Publications, vol. 268, pp. 25–37.

Grujic, D., Hollister, L.S., Parrish, R.R., 2002. Himalayan metamorphic sequence as an orogenic channel: insight from Bhutan. Earth and Planetary Science Letters 198, 177–191.

Grujic, D., Martin, C., Davidson, C., Hollister, L.S., Kuendig, R., Pavlis, T.L., Schmid, S.M., 1996. Ductile extrusion of the Higher Himalayan Crystalline in Bhutan; evidence from quartz microfabrics. Tectonophysics 260, 21–43.

Guillot, S., Garzanti, E., Baratoux, D., Marquer, D., Maheo, G., de Sigoyer, J., 2003. Reconstructing the total shortening history of the NW Himalaya. Geochemistry, Geophysics, Geosystems 4, 1–50.

Hager, C., Stockli, D.F., Dewane, T.J., Ding, L., 2006. Episodic Mio-Pliocene rifting in south-central Tibet. Thermochronometric constraints from the Xainza rift. Eos (Transactions, American Geophysical Union) 87 T34C-02.

Hirth, G., Teyssier, C., Dunlap, J., 2001. An evaluation of quartzite flow laws based on comparisons between experimentally and naturally deformed rocks. International Journal of Earth Sciences 90, 77–87.

Hirth, G., Tullis, J., 1992. Dislocation creep regimes in quartz aggregates. Journal of Structural Geology 14, 145–159.

Hodges, K.V., Hurtado, J.M., Whipple, K.X., 2001. Southward extrusion of Tibetan crust and its effect on Himalayan tectonics. Tectonics 20, 799–809.

Jessell, M.W., 1987. Grain-boundary migration microstructures in a naturally deformed quartzite. Journal of Structural Geology 9, 1007–1014.

Jessup, M.J., Law, R.D., Frassi, C., 2007. The rigid grain net (RGN): an alternative method for estimating mean kinematic vorticity number (W_m). Journal of Structural Geology 29, 411–421.

Jessup, M.J., Law, R.D., Searle, M.P., Hubbard, M.S., 2006. Structural evolution and vorticity of flow during extrusion and exhumation of the Greater Himalayan Slab, Mount Everest Massif, Tibet/Nepal: implications for orogen-scale flow partitioning. In: Law, R.D., Searle, M.P., Godin, L. (Eds.), Channel Flow, Ductile Extrusion and Exhumation in Continental Collision Zones. Geological Society, London, Special Publications, vol. 268, pp. 379–413.

Jiang, D., 1998. Forward modeling of non-steady-state deformations and the 'minimum strain path': discussion. Journal of Structural Geology 20, 975–977.

Kawakami, T., Aoya, M., Wallis, S.R., Lee, J., Terada, K., Wang, Y., Heizler, M., 2007. Contact metamorphism in the Malashan dome, North Himalayan gneiss domes, southern Tibet: an example of shallow extensional tectonics in the Tethys Himalaya. Journal of Metamorphic Geology 25, 831–853.

Kruhl, J.H., 1998. Reply: prism- and basal-plane parallel subgrain boundaries in quartz: a Microstructural geothermometer. Journal of Metamorphic Petrology 16, 142–146.

Law, R.D., Morgan, S.S., Casey, M., Sylvester, C.M., Nyman, M., 1992. The Papoose Flat pluton of eastern California: a re-assessment of its emplacement history in the light of new microstructural and crystallographic fabric observations. Transactions of the Royal Society of Edinburgh: Earth Sciences 83, 361–375.

Law, R.D., 1990. Crystallographic fabrics: a selective review of their applications to research in structural geology. In: Knipe, R.J., Rutter, E.H. (Eds.), Deformation Mechanisms, Rheology and Tectonics. Geological Society, London, Special Publications, vol. 54, pp. 335–352.

Law, R.D., Searle, M.P., Simpson, R.L., 2004. Strain, deformation temperatures and vorticity of flow at the top of the Greater Himalayan Slab, Everest Massif, Tibet. Journal of the Geological Society of London 161, 305–320.

Lee, J., Dinklage, W.S., Hacker, B.R., Wang, Y., Gans, P.B., Calvert, A., Wan, J., Chen, W., Blythe, A., McClelland, W., 2000. Evolution of the Kangmar Dome, southern Tibet: structural, petrologic, and thermochronologic constraints. Tectonics 19, 872–896.

Lee, J., Dinklage, W.S., Wang, Y., Wan, J., 2002. Geology of the Kangmar Dome, southern Tibet with explanatory notes. In: Geological Society of America Map and Chart Series MCH090, 1:50,000 Scale, 8 pp.

Lee, J., Hacker, B., Wang, Y., 2004. Evolution of North Himalayan gneiss domes: structural and metamorphic studies in Mabja Dome, southern Tibet. Journal of Structural Geology 26, 2297–2316.

Lee, J., McClelland, W., Wang, Y., Blythe, A., McWilliams, M., 2006. Oligocene–Miocene middle crustal flow in the southern Tibet: geochronology of Mabja Dome. In: Law, R.D., Searle, M.P., Godin, L. (Eds.), Channel Flow, Ductile Extrusion and Exhumation in Continental Collision Zones. Geological Society, London, Special Publications, vol. 268, pp. 445–469.

Lee, J., Whitehouse, M.J., 2007. Onset of mid-crustal extensional flow in southern Tibet: evidence from U/Pb zircon ages. Geology 35, 45–48.

Leech, M.L., Singh, S., Jain, A.K., Klemperer, S.L., Manickavasagam, R.M., 2005. The onset of India-Asia continental collision: early, steep subduction required by the timing of UHP metamorphism in the western Himalaya. Earth and Planetary Science Letters 234, 83–97.

Le Fort, P., 1975. Himalayas; the collided range; present knowledge of the continental arc. American Journal of Science 275-A, 1–44.

Lister, G.S., Dornsiepen, U.F., 1982. Fabric transitions in the Saxony granulite terrain. Journal of Structural Geology 4, 81–93.

Lister, G.S., Hobbs, B.E., 1980. The simulation of fabric development during plastic deformation and its application to quartzite: the influence of deformation history. Journal of Structural Geology 2, 355–370.

Lister, G.S., Paterson, M.S., Hobbs, B.E., 1978. The simulation of fabric development in plastic deformation and its application to quartzite; the model. Tectonophysics 45, 107–158.

Liu, G., Einsele, G., 1994. Sedimentary history of the Tethyan basin in the Tibetan Himalayas. Geologische Rundschau 82, 32–61.

Lloyd, G.E., Freeman, B., 1994. Dynamic recrystallization of quartz under greenschist conditions. Journal of Structural Geology 16, 867–881.

Mainprice, D., Bouchez, J.L., Blumenfeld, P., Tubia, J.M., 1986. Dominant c slip in naturally deformed quartz: implications for dramatic plastic softening at high temperature. Geology 14, 819–822.

Mancktelow, N.S., 1995. Nonlithostatic pressure during sediment subduction and the development and exhumation of high pressure metamorphic rocks. Journal of Geophysical Research 100, 571–583.

Molnar, P., England, P., Martinod, J., 1993. Mantle dynamics, uplift of the Tibetan plateau, and the Indian monsoon. Reviews of Geophysics 31, 357–396.

Murphy, M.A., Harrison, T.M., 1999. Relationship between leucogranites and the Qomolangma detachment in the Rongbuk Valley, south Tibet. Geology 27, 831–834.

Nyman, M.W., Law, R.D., Morgan, S.S., 1995. Conditions of contact metamorphism, Papoose Flat Pluton, eastern California, USA: implications for cooling and strain histories. Journal of Metamorphic Geology 13, 627–643.

Nelson, K.D., Zhao, W., Brown, L.D., Kuo, J., Che, J., Liu, X., Klemperer, S.L., Makovsky, Y., Meissner, R., Mechie, J., Kind, R., Wenzel, F., Ni, J., Nabelek, J., Chen, L., Tan, H., Wei, W., Jones, A.G., Booker, J., Unsworth, M., Kidd, W.S.F., Hauck, M., Alsdorf, D., Ross, A., Cogan, M., Wu, C., Sandvol, E.A., Edwards, M., 1996. Partially molten middle crust beneath southern Tibet: Synthesis of project INDEPTH results. Science 274, 1684–1688.

Okudaira, T., Takesbita, T., Hara, I., Ando, J., 1995. A new estimate of the conditions for transition from basal <a> to prism [c] slip in naturally deformed quartz. Tectonophysics 250, 31–46.

Passchier, C.W., 1987. Stable positions of rigid objects in non-coaxial flow: a study in vorticity analysis. Journal of Structural Geology 9, 679–690.

Passchier, C.W., Trouw, R.A.J., 2005. Microtectonics. Springer Berlin Heidelberg, New York.

Pfiffner, A.O., Ramsay, J.G., 1982. Constraints on geological strain rates: arguments from finite strain states of naturally deformed rocks. Journal of Geophysical Research 87, 311–321.

Pryer, L.L., 1993. Microstructures in feldspars from a major crustal thrust zone: the Grenville Front, Ontario, Canada. Journal of Structural Geology 15, 21–36.

Quigley, M., Liangjun, Y., Gregory, C., Corvino, A., Sandiford, M., Wilson, C.J.L., Xiaohan, L., 2008. U/Pb SHRIMP zircon geochronology and T-t-d history of the Kampa Dome, southern Tibet: implications for tectonic evolution of the North Himalayan gneiss domes. Tectonophysics 446, 97–113.

Quigley, M., Liangjun, Y., Xiaohan, L., Wilson, C.J.L., Sandiford, M., Phillips, D., 2006. ^{40}Ar/^{39}Ar thermochronology of the Kampa Dome, southern Tibet; implications for tectonics evolution of the North Himalayan gneiss domes. Tectonophysics 421, 269–297.

Ramsay, J.G., Huber, M.I., 1987. The Techniques of Modern Structural Geology Volume 2: Folds and Fractures. Academic Press, London.

Rasband, W.S., 2005. ImageJ 1.34, [Computer Software]. U.S. National Institute of Health, Bethesda, MD.

Ratschbacher, L., Frisch, W., Liu, G., Chen, C., 1994. Distributed deformation in southern and western Tibet during and after the India-Asia collision. Journal of Geophysical Research 99, 19917–19945.

Rowley, D.B., Currie, B.S., 2006. Paleo-altimetry of the late Eocene to Miocene Lunpola basin, central Tibet. Nature 439, 677–681.

Searle, M.P., Simpson, R.L., Law, R.D., Parrish, R.R., Waters, D.J., 2003. The structural geometry, metamorphic and magmatic evolution of the Everest massif, High Himalaya of Nepal-South Tibet. Journal of the Geological Society of London 160, 345–366.

Selverstone, J., 2005. Preferential embrittlement of graphitic schists during extensional unroofing in the Alps: the effect of fluid composition on rheology in low-permeability rocks. Journal of Metamorphic Geology 23, 461–470.

Simpson, C., 1985. Deformation of granitic rocks across the brittle–ductile transition. Journal of Structural Geology 7, 503–511.

Simpson, R.L., Parrish, R.R., Searle, M.P., Waters, D.J., 2000. Two episodes of monazite crystallization during metamorphism and crustal melting in the Everest region of the Nepalese Himalaya. Geology 28, 403–406.

Spear, F., Menard, T., 1989. Program GIBBS: a generalized Gibbs method algorithm. American Mineralogist 74, 942–943.

Stipp, M., Stünitz, H., Heilbronner, R., Schmid, S.M., 2002a. The eastern Tonale fault zone: a 'natural laboratory' for crystal plastic deformation of quartz over a temperature range from 250 to 700 °C. Journal of Structural Geology 24, 1861–1884.

Stipp, M., Stünitz, H., Heilbronner, R., Schmid, S.M., 2002b. Dynamic recrystallization of quartz: correlation between natural and experimental conditions. In: De Meer, S., Drury, M.R., De Bresser, J.H.P., Pennock, G.M. (Eds.), Deformation Mechanisms, Rheology and Tectonics: Current Status and Future Perspectives. Geological Society, London, Special Publications, vol. 200, pp. 171–190.

Stockli, D.F., Taylor, M., Yin, A., Harrison, T.M., D'Andrea, J., Lin, D., Kapp, P., 2002. Late Miocene–Pliocene inception of E–W extension in Tibet as evidenced by apatite (U–Th)/He data. Geological Society of America Abstracts with Programs 34, 411.

Tullis, J., Christie, J.M., Griggs, D.T., 1973. Microstructures and preferred orientations of experimentally deformed quartzites. Geological Society of America Bulletin 84, 297–314.

Tullis, J., Yund, R., 1992. The brittle–ductile transition in feldspar aggregates: an experimental study. In: Evans, B., Wong, T.F. (Eds.), Fault Mechanics and Transport Properties in Rocks. Academic Press, New York, pp. 89–118.

Turcotte, D., Schubert, G., 2002. Geodynamics. Cambridge University Press.

Vance, D., Harris, N., 1999. The timing of prograde metamorphism in the Zanskar Himalaya. Geology 27, 395–398.

Vannay, J.-C., Grasemann, B., 1998. Inverted metamorphism in the High Himalaya of Himachal Pradesh (NW India): phase equilibria versus thermobarometry. Schweizerische Mineralogische und Petrographische Mitteilungen 78, 107–132.

Vannay, J.-C., Grasemann, B., 2001. Himalayan inverted metamorphism and syn-convergence extension as a consequence of a general shear extrusion. Geological Magazine 138, 253–276.

Walker, J.D., Martin, M.W., Bowring, S.A., Searle, M.P., Waters, D.J., Hodges, K.V., 1999. Metamorphism, melting, and extension: age constraints from the High Himalayan slab, S.E. Zanskar and N.W. Lahoul. Journal of Geology 107, 473–495.

Wallis, S.R., Platt, J.P., Knott, S.D., 1993. Recognition of syn-convergence extension in accretionary wedges with examples from the Calabrian Arc and the Eastern Alps. American Journal of Science 293, 463–495.

Wenk, H.R., Canova, G., Molinari, A., Kocks, U.F., 1989. Viscoplastic modeling of texture development in quartzite. Journal of Geophysical Research 94, 17895–17906.

White, F.M., 1974. Viscous Fluid Flow. McGraw-Hill, New York, 725 pp.

Wu, C., Nelson, K.D., Wortman, G., Samson, S.D., Yue, Y., Li, J., Kidd, W.S.F., Edwards, M.A., 1998. Yadong cross structure and South Tibetan detachment in the east central Himalaya (89°–90°E). Tectonics 17, 28–45.

Zhang, H., Harris, N., Parrish, R., Kelley, S., Zhang, L., Rogers, N., Argles, T., King, J., 2004. Causes and consequences of protracted melting of the mid-crust exposed in the North Himalayan antiform. Earth and Planetary Science Letters 228, 195–212.